

8-1-2016

Visualization of dropwise condensation on vertical plate and horizontal tube geometry

Blake Naccarato

University of Nevada, Las Vegas, blake.naccarato@gmail.com

Follow this and additional works at: <https://digitalscholarship.unlv.edu/thesesdissertations>



Part of the [Mechanical Engineering Commons](#)

Repository Citation

Naccarato, Blake, "Visualization of dropwise condensation on vertical plate and horizontal tube geometry" (2016). *UNLV Theses, Dissertations, Professional Papers, and Capstones*. 3093.
<https://digitalscholarship.unlv.edu/thesesdissertations/3093>

This Thesis is protected by copyright and/or related rights. It has been brought to you by Digital Scholarship@UNLV with permission from the rights-holder(s). You are free to use this Thesis in any way that is permitted by the copyright and related rights legislation that applies to your use. For other uses you need to obtain permission from the rights-holder(s) directly, unless additional rights are indicated by a Creative Commons license in the record and/or on the work itself.

This Thesis has been accepted for inclusion in UNLV Theses, Dissertations, Professional Papers, and Capstones by an authorized administrator of Digital Scholarship@UNLV. For more information, please contact digitalscholarship@unlv.edu.

VISUALIZATION OF DROPWISE CONDENSATION ON VERTICAL PLATE AND
HORIZONTAL TUBE GEOMETRY

By

Blake Naccarato

Bachelor of Science in Engineering – Mechanical Engineering
University of Nevada, Las Vegas
2014

A thesis submitted in partial fulfillment
of the requirements for the

Master of Science in Engineering – Mechanical Engineering

Department of Mechanical Engineering
Howard R. Hughes College of Engineering
The Graduate College

University of Nevada, Las Vegas
August 2017



Thesis Approval

The Graduate College
The University of Nevada, Las Vegas

July 10, 2017

This thesis prepared by

Blake Naccarato

entitled

Visualization of Dropwise Condensation on Vertical Plate and Horizontal Tube
Geometry

is approved in partial fulfillment of the requirements for the degree of

Master of Science in Engineering – Mechanical Engineering
Department of Mechanical Engineering

Kwang Kim, Ph.D.
Examination Committee Chair

Kathryn Hausbeck Korgan, Ph.D.
Graduate College Interim Dean

Robert Boehm, Ph.D.
Examination Committee Member

Woosoon Yim, Ph.D.
Examination Committee Member

Daniel Gerrity, Ph.D.
Graduate College Faculty Representative

Abstract

A droplet detection method has been developed to measure the distribution of droplet sizes on a flat plate under dropwise condensation. Dropwise condensation heat transfer may be modeled by combining an expression for the single droplet heat transfer rate with the droplet size distribution. The ability to measure this distribution is integral to the validation of such models. An example study is undertaken in which heat flux is obtained for a given surface treatment by implementing such a model and measuring the droplet size distribution. These results are compared with the heat flux measured by internal coolant temperature monitoring for external condensation on a tube featuring the same surface treatment.

The plate condensing heat exchanger is a modular design for condensate visualization. The core of the design is a four-way pipe cross with open flanges on each end. Flange caps are designed to accomplish the goal of condensate visualization, and are easily exchangeable depending on design intent. The sample side flange features a conductive contact between an external cold plate and internally-mounted sample. A viewing flange opposite the sample side flange allows for lighting and capture of video data of the condensation process. A third flange features an internal, concentric boiler for steam generation. A vacuum pump valve and ambient temperature and pressure sensors are fitted to the fourth flange cap. Dropwise condensation models are explored in this setup by detection of droplets in the captured video data.

Droplet detection is performed by a Circle Hough Transform that has been modified to handle the order-of-magnitude differences in droplet radii within the same image. The Circle Hough Transform is applied to detect a radius range corresponding to the largest droplets, then the next largest droplets, and so on until the smallest detectable droplets have been marked. Detections in any given stage of the modified Circle Hough Transform are used to mask the

detection region for the next stage. This reduces detection noise emanating from larger droplets that would otherwise overwhelm detections of smaller droplets. Another technique used in reducing detection noise involves illumination leveling, morphological erosion, and morphological reconstruction of the video data. The combination of these methods yield measurements of the droplet size distribution suitable for heat transfer analysis.

The droplet size distribution is dependent upon a balance between droplet growth and sweeping of condensate, which is observable by analyzing the distribution in each frame of the video data. While the distribution is constant for very large condensing surfaces, the local droplet size distribution varies as droplets nucleate, grow, coalesce, and are swept away by departing droplets. This apparatus and detection method make it possible to observe time-dependent growth and sweeping mechanisms as well as the droplet size distribution that emerges from these mechanisms. This study demonstrates the utility of the apparatus and detection method for the validation of dropwise condensation heat transfer models.

Acknowledgements

I would like to thank my advisor, Dr. Kwang Kim, for his support throughout my graduate studies. I appreciate the guidance given in my research, as well as his financial support throughout. I am also grateful for the opportunities he has provided for me to travel to a research lab and engineering conference. These opportunities have helped me to understand the nature of research in a broader context.

I would also like to thank Dr. Robert Boehm, Dr. Daniel Gerrity, and Dr. Woosoon Yim for their advisement and for serving as members of my committee. I am grateful for their interest in my research.

I would like to thank Dr. Kuok Cheng and Mike Kennedy for their help in setting up Dr. Cheng's tube condensing heat exchanger. I would like to thank others who have helped me, including machinists Tony Filipiak and Terry Kell for making my design a reality, Rick Hurt for his consultation and help with a troublesome pipe fitting, and Jeffery Markle for his assistance in data acquisition. I am also grateful to my colleagues in the Active Materials and Smart Living lab. I am grateful for their design support, as well as for their help transporting my fifty-kilogram heat exchanger on more than one occasion.

This work was in part supported by NASA (NNX15AM77A). I also received the Higher Education Fellowship grant from the Nevada NASA Space Grant Consortium (NVSGC) for two semesters of my graduate study. I am grateful to NVSGC for this support, as well as the 1:1 match provided by Dr. Kwang Kim.

Finally, I would like to acknowledge the support of my family and my girlfriend. Their encouragement is part of the reason I chose to pursue graduate studies in the first place, and their continued support has helped me along the way.

Table of Contents

Abstract.....	iii
Acknowledgements.....	v
List of Figures.....	viii
Nomenclature.....	x
Chapter 1. Introduction.....	1
Chapter 2. Theoretical Consideration.....	5
2.1. Single Droplet Heat Transfer.....	5
2.2. Large Droplet Size Distribution.....	7
2.3. Small Droplet Size Distribution.....	10
2.4. Heat Flux and Equivalent Heat Transfer Coefficient.....	12
Chapter 3. Experimental Setup.....	14
3.1. Plate Condensing Heat Exchanger (PC-HEX).....	14
3.1.1. Apparatus.....	14
3.1.1. Handling of Noncondensable Gases.....	18
3.1.2. Experimental Method.....	20
3.2. Tube Condensing Heat Exchanger (TC-HEX).....	23
3.2.1. Apparatus.....	23
3.2.2. Experimental Method.....	27
Chapter 4. Data Handling.....	29
4.1. PC-HEX Data.....	29
4.1.1. Droplet Detection.....	29
4.1.2. Video Processing.....	36

4.1.3. Relating Measurements to Theory	39
4.1.4. Measurement Uncertainty	42
4.2. TC-HEX Data	44
4.2.1. Relating Measurements to Theory	44
4.2.2. Measurement Uncertainty	48
Chapter 5. Results	50
5.1. PC-HEX	50
5.2. Interpretation of Theory	55
5.3. TC-HEX	59
5.4. Measurement Uncertainty	60
Chapter 6. Conclusion	63
6.1. Relevance of Current Study	63
6.2. Future Study	64
6.3. Final Remark	66
Appendix A: PC-HEX Numerical Data	68
Appendix B: Video Data from the PC-HEX and TC-HEX Apparatuses	71
Bibliography	72
Curriculum Vitae	75

List of Figures

Figure 1. Filmwise and Dropwise Condensation on Horizontal Tube.....	4
Figure 2. Condensate Droplet Model.....	5
Figure 3. Representation of Area Fractions	9
Figure 4. PC-HEX Design Render.....	15
Figure 5. PC-HEX Sample Side Flange.....	16
Figure 6. PC-HEX Sample Mounted to Copper Plug.....	17
Figure 7. PC-HEX Boiler Flange.....	18
Figure 8. PC-HEX Pump Side Flange	19
Figure 9. PC-HEX Apparatus	19
Figure 10. LabVIEW Block Diagram for PC-HEX Data Acquisition.....	21
Figure 11. PC-HEX High-Speed Camera and Data Acquisition Setup	22
Figure 12. TC-HEX Apparatus	24
Figure 13. TC-HEX Process Diagram	25
Figure 14. TC-HEX Inlet Coolant Line	26
Figure 15. TC-HEX Instrumentation	27
Figure 16. Image of Coins and Prominent Edges	30
Figure 17. Examples of Single Voter and Vote Weights.....	33
Figure 18. Quarter and Nickel Detection Stages	34
Figure 19. Penny and Dime Detection Stages	35
Figure 20. Background Handling Process	38
Figure 21. Detection Region and Glare Removal Process.....	38
Figure 22. Droplet Detections during Droplet Sweeping Event.....	38

Figure 23. Thermal Resistances for Plate Geometry	41
Figure 24. Equivalent Untreated Plate Model.....	42
Figure 25. TC-HEX Tube Sample Cross-Section.....	45
Figure 26. Thermal Resistances for Tube Geometry	47
Figure 27. Processed Video Frames Highlighting Droplet Sweeping Event.....	50
Figure 28. Droplet Count Density and Sweeping Events Over Time.....	51
Figure 29. Droplet Size Distribution and Single Droplet Heat Transfer Rate	52
Figure 30. Instantaneous and Mean Heat Flux	54
Figure 31. Instantaneous and Mean Equivalent Heat Transfer Coefficient.....	55
Figure 32. Droplet Distribution and Ratio for Increasing Contact Angle.....	57
Figure 33. Single Droplet Heat Transfer and the Heat Flux Distribution.....	58
Figure 34. Heat Flux and Equivalent Heat Transfer Coefficient for PC-HEX Tube Samples	61
Figure 35. Frame from High-Speed Video Data of PC-HEX Samples	62
Figure 36. PC-HEX Chamber Undisturbed Pressure.....	68
Figure 37. Full Experimental Run for First PC-HEX Sample	69
Figure 38. Full Experimental Run for Second PC-HEX Sample.....	70

Nomenclature

a	Projected droplet area (m ²)	g_y	Image y-directional gradient at current pixel
A_s	Condensing surface area (m ²)		
$A(r)$	Surface area covered by droplets with radii between r and $(r + dr)$ (m ²)	h_c	Heat transfer coefficient of the PC-HEX coolant (W/m ² K)
b	Power index in the large droplet size distribution	h_{eq}	Equivalent heat transfer coefficient (W/m ² K)
b_{mod}	Power index resulting from nonlinear fit to measured droplet size distribution	$h_{eq,meas}$	Measured equivalent heat transfer coefficient (W/m ² K)
$c_{p,c}$	Specific heat of the condensate (J/kg-K)	$h_{eq,mod}$	Equivalent heat transfer coefficient modified for additional temperature drops (W/m ² -K)
δ	Coating thickness (m)	H_{fg}	Enthalpy of vaporization of water (J/kg)
ΔT	Subcool temperature (K)	h_i	Heat transfer coefficient at the liquid-vapor interface (K)
ΔT_c	Temperature drop across the PC-HEX coolant (K)	i	x-coordinate of current pixel
ΔT_{coat}	Temperature drop across the coating (K)	I	grayscale intensity of current pixel
ΔT_{curv}	Temperature drop due to droplet curvature (K)	j	y-coordinate of current pixel
ΔT_{drop}	Temperature drop through the droplet (K)	Ja	Jacob number
ΔT_i	Temperature drop at the liquid-vapor interface (K)	k	Thermal conductivity of the plate/tube (W/mK)
ΔT_{mod}	Measured temperature drop in either the PC-HEX or TC-HEX apparatus (K)	k_c	Thermal conductivity of the condensate (W/mK)
ΔT_p	Temperature drop across the plate (K)	k_{coat}	Thermal conductivity of the coating (W/mK)
ΔT_t	Temperature drop across the tube (K)	k_w	Thermal conductivity of the PC-HEX chamber wall (K)
ΔT_w	Temperature drop across the PC-HEX chamber wall (K)	L	Length of the PC-HEX tube sample (m)
f	Fraction of surface area covered by droplets with radii greater than r	M	Magnitude of a vote in the Circle Hough Transform
g	Image gradient magnitude at current pixel	\dot{m}_c	Mass flow rate of coolant in the PC-HEX tube sample (kg/s)
g_x	Image x-directional gradient at current pixel	μ	Condensate viscosity (Pa-s)
		n	Small droplet size distribution (m ³)
		n_{mod}	Modified small droplet size distribution (m ⁻³)
		N_s	Nucleation site density (m ⁻²)

N	Large droplet size distribution (m^{-3})	S	Surface renewal rate (m^2/s)
N_{mod}	Large droplet size distribution with modified power index b_{mod} (m^{-3})	σ	Surface tension of the condensate (N/m)
ϕ	Radius encoded as phase in Circle Hough Transform	t	Plate thickness (m)
ϕ_{avg}	Average phase as a result of multiple votes on one pixel	$T_{c,ave}$	Average coolant temperature (K)
q_d	Single droplet heat transfer rate (W)	$T_{c,i}$	Inlet coolant temperature (K)
$q_{d,mod}$	Single droplet heat transfer rate modified for additional temperature drops (W)	$T_{c,o}$	Outlet coolant temperature (K)
q''	Heat flux (W/m^2)	T_s	Temperature at surface just beneath coating (K)
q''_{meas}	Measured heat flux (W/m^2)	T_{sat}	Saturated steam temperature (K)
q''_{mod}	Heat flux modified for additional temperature drops (W/m^2)	t_w	PC-HEX chamber wall thickness (m)
r	Droplet radius (m)	τ	Sweeping period (s)
r_{avg}	Average radius as a result of multiple votes on one pixel (m)	θ	Water contact angle ($^\circ$)
r_e	Radius at which droplets begin to coalesce due to being larger than the nucleation site density (m)	T_w	PC-HEX chamber wall temperature (K)
r_{est}	Radius estimate for circle detection (m)	$u_{\Delta T}$	Relative uncertainty in subcool temperature (K)
$r_{est,max}$	Maximum radius estimate for circle detection (m)	$u_{\Delta T_c}$	Relative uncertainty in coolant temperature difference (K)
$r_{est,min}$	Minimum radius estimate for circle detection (m)	$u_{h_{eq,meas}}$	Relative uncertainty in heat transfer coefficient (K)
r_i	PC-HEX inner tube outer radius (m)	$u_{q''_{meas}}$	Relative uncertainty in heat flux (K)
r_{max}	Maximum droplet radius before departing under its own weight (m)	$U_{q_{d,meas}}$	Absolute uncertainty in single droplet heat transfer rate (W)
r_{min}	Minimum thermodynamically viable droplet radius (m)	u_r	Relative uncertainty in droplet radius
r_o	PC-HEX outer tube outer radius (m)	U_r	Absolute uncertainty in droplet radius (m)
ρ	Density of condensate (kg/m^3)	w	Complex weight function for the Circle Hough Transform
ρ_g	Density of steam (kg/m^3)	x_{est}	Estimate of circle center x-location
		y_{est}	Estimate of circle center y-location
		x_{voter}	x-coordinate of voter pixel
		y_{voter}	y-coordinate of voter pixel

Chapter 1. Introduction

The effectiveness of condensation heat transfer to a surface is affected by the type of condensation that occurs. The two types of condensation considered in this study are shown in **Figure 1**. Heat transfer is shown to improve in dropwise condensation compared to filmwise condensation [1,2]. In filmwise condensation, steam condenses onto a surface in the form of a film. This is the case with steam condensation onto an untreated, metal surface. The condensate has high thermal resistance compared to the condensing surface and acts as an insulator. This flooding of the surface prevents direct condensation to the substrate. In dropwise condensation, as discovered by Schmidt et al. [3], droplets form at microscale imperfections on the surface called nucleation sites. Direct condensation to droplets causes them to grow. Droplets that grow large enough to intersect will coalesce. Droplets continue to grow and coalesce until some become large enough to depart the surface under the influence of gravity. Departing droplets sweep away any condensate in their path, freeing up nucleation sites for more droplets to form. This process has a lower effective thermal resistance than that of filmwise condensation because a greater fraction of the substrate is exposed at any given time.

Dropwise condensation can be promoted by making the condensing surface more hydrophobic. Khandekar and Muralidhar [4] provide a good overview of hydrophobicity as it relates to dropwise condensation. A surface is hydrophobic if the contact angle that a water droplet makes with the surface is greater than 90° . The definition of the contact angle can be seen in **Figure 2** (see page 5). Thomas Young [5] describes the formation of a water contact angle in terms of the surface energies of the substrate, fluid, and surrounding vapor. Subsequent works by Wenzel [6] and Cassie and Baxter [7] sought to define the effect of surface microstructure on hydrophobicity. Dettre and Johnson [8,9] explore the importance of contact angle hysteresis on

wettability. Contact angle hysteresis is the difference in contact angle between a growing and shrinking droplet. Yaminsky [10] attributes this range of observed contact angles to droplet contact-line pinning due to surface roughness. Surface treatments that increase the contact angle and decrease contact angle hysteresis tend to promote dropwise condensation.

A variety of surface modifications have been found to promote dropwise condensation. Enright et al. [11] provide a review of various techniques. Self-assembled monolayers are atom-thick surface treatments that show good hydrophobicity [12–15]. These can be compared with thicker polymer coatings of PTFE and PPS [14]. Rare-earth oxides have also been shown to be hydrophobic and relatively weatherable by Azimi et al. [16]. Techniques involving microelectromechanical systems (MEMS) also yield hydrophobic surfaces, such as the one described by Huang and Leu [17]. Hydrophobic surface preparation by laser irradiation techniques is demonstrated out by Lee et al. [18]. Promotion of hydrophobicity also has applications in the medical field and for discouraging surface icing. For the former, Movafaghi et al. [19] show that titania surfaces are hemophobic and may reduce platelet adhesion. Guo et al. [20] present the latter with icephobic surfaces formed by a combination of machining and crystal growth.

Various models of dropwise condensation heat transfer have been proposed [1,2,21–23]. These approaches involve the combination of heat transfer through a single droplet with a model of the population of droplets on the surface, called the droplet size distribution. LeFevre and Rose [2] propose a distribution that defines the number of droplets of a given radius per unit area of condensing surface. The form of this distribution has since been verified by experimental results [24–26]. The droplet size distribution was explored further by Tanaka [27]. The results by Tanaka are backed up by Neumann [28] and Maa [29], who show that small droplets contribute

to heat transfer. Small droplets are those which are too small to coalesce with their nearest neighbors. This is because droplets must form at nucleation sites on the surface. If the nucleation site density can be assumed to be uniform, then droplets smaller than the distance between nucleation sites cannot coalesce. Kim and Kim [23] also propose a droplet size distribution that accounts for such droplets. Individual droplet heat transfer is explored by Fatica and Katz [22], who find an expression for thermal conduction through a single droplet by integrating across isothermal surfaces between the droplet base and cap. Recently, Kim and Kim [23] found an analytical result to this problem. Summing the heat transfer rates of individual droplets according to the droplet size distribution yields the expected heat flux through the condensing surface.

Two external condensation experiments are used to explore heat transfer and visualize condensation on hydrophobic surfaces. One is a tube condensing heat exchanger with carefully monitored coolant conditions inside the tube sample and ambient conditions in the surrounding chamber. This apparatus was originally developed for the study of external condensation on a horizontal tube by Cheng [30]. The second is a plate condensing heat exchanger with a large viewport to the condensing surface of the plate sample. This apparatus has been developed specifically for this study. The former apparatus allows for measurement of heat flux by inlet-outlet coolant temperature monitoring, while the latter is used to measure the droplet size distribution on a flat plate. These two apparatuses are used to explore population-based models of dropwise condensation heat transfer.

In this work, the droplet size distribution is measured in the flat plate heat exchanger by applying a circle detection method to images of active dropwise condensation on the sample surface. The method employed in this study is a modified form of the Circle Hough Transform [31,32]. The basic method has been modified to allow for detection of a wide range of

droplet sizes. The measured droplet size distribution is used to explore time-dependent characteristics of dropwise condensation and to inform an estimate of heat flux. The measured droplet size distribution is combined with a model of individual droplet heat transfer to yield estimates of the heat flux and equivalent heat transfer coefficient. These estimates are compared with measurements of heat flux from the tube condensing heat exchanger for the same surface treatment.



Figure 1. Filmwise and Dropwise Condensation on Horizontal Tube

Top: Filmwise condensation on horizontal tube. *Bottom:* Dropwise condensation on horizontal tube.

Chapter 2. Theoretical Consideration

A theory of heat flux for condensation heat transfer is obtained from a combination of individual droplet heat transfer and the droplet size distribution. The heat flux laid out here neglects thermal resistances beneath a surface coating, so it defines a maximum obtainable heat flux for any given application of the coating. Heat flux measurements on a plate and tube geometry are compared with this maximum expected heat flux.

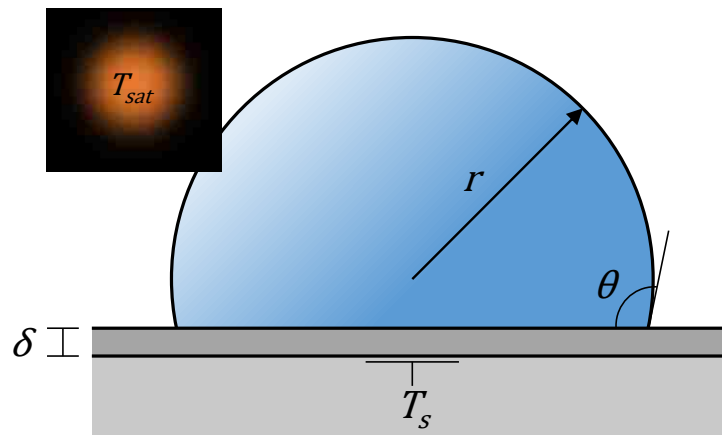


Figure 2. Condensate Droplet Model

The condensate droplet is assumed to take the shape of a spherical cap with radius r and contact angle θ . The coating thickness is δ . The subcool temperature ΔT is the difference between saturation temperature T_{sat} and surface temperature T_s .

2.1. Single Droplet Heat Transfer

Various models of the heat transfer through a single droplet have been proposed [1,2,22,23]. These models define four temperature drops between ambient conditions and the substrate that make up the subcool temperature ΔT , which is the difference between T_{sat} and T_s in **Figure 2**. The condensate droplet is assumed to take the shape of a spherical cap. The subcool temperature ΔT is as follows

$$\Delta T = \Delta T_i + \Delta T_{curv} + \Delta T_{drop} + \Delta T_{coat} \quad (2.1)$$

where ΔT_i , ΔT_{curv} , ΔT_{drop} , and ΔT_{coat} are the temperature drops across the liquid-steam interface, due to droplet curvature, across the droplet, and across the coating, respectively. While Fatica and Katz [22] use numerical integration to model ΔT_{drop} , Kim and Kim [23] have obtained it analytically. The latter method is used to model temperature drop through the droplet. The temperature drops in Equation 2.1 are defined in [23]

$$\Delta T_i = \frac{q_d}{h_i 2\pi r^2 (1 - \cos \theta)} \quad (2.2)$$

$$\Delta T_{curv} = \frac{r_{min} \Delta T}{r} \quad (2.3)$$

$$\Delta T_{drop} = \frac{q_d \theta}{4\pi r k_c \sin \theta} \quad (2.4)$$

$$\Delta T_{coat} = \frac{q_d \delta}{k_{coat} \pi r^2 \sin^2 \theta} \quad (2.5)$$

where q_d is the single droplet heat transfer rate, and ΔT_{curv} is provided by LeFevre and Rose [2]. The interfacial heat transfer coefficient h_i is reported by Tanasawa [33] to vary from 0.383 MW/m²K to 15.7 MW/m²K for 0.01 atm to 1.0 atm. A PTFE-based coating is used in this experiment. Its thermal conductivity k_{coat} is 0.30 W/mK [34]. Its thickness δ is 12.7 μ m. The contact angle θ is 165°. r_{min} is the minimum thermodynamically viable droplet radius [35]

$$r_{min} = \frac{2T_{sat}\sigma}{H_{fg}\rho\Delta T} \quad (2.6)$$

where T_{sat} is the saturated steam temperature, σ is the surface tension, H_{fg} is the enthalpy of vaporization of water, and ρ is the density of water. Substituting Equations 2.2 – 2.5 into Equation 2.1 yields the following

$$q_d = \frac{\Delta T \pi r^2 \left(1 - \frac{r_{min}}{r}\right)}{\frac{\delta}{k_{coat} \sin^2 \theta} + \frac{r\theta}{4k_c \sin \theta} + \frac{1}{2h_i(1 - \cos \theta)}} \quad (2.7)$$

The heat transfer rate through a single droplet is obtained. The sum of heat transfer rates through the entire population of droplets on a surface yields the heat flux through that surface. This requires a model of the expected droplet size distribution.

2.2. Large Droplet Size Distribution

The preceding single-droplet model is combined with a model of the droplet size distribution. The model by LeFevre and Rose [2] begins with a function that defines the fraction of surface area covered by droplets of radius r and greater, and its derivative

$$f(r) = 1 - \left(\frac{r}{r_{max}}\right)^b \quad (2.8)$$

$$f'(r) = -\frac{b}{r} \left(\frac{r}{r_{max}}\right)^b \quad (2.9)$$

where r_{max} is the largest droplet size that can exist on the surface before departing due to gravity. The area fractions utilized in this theory are visualized for a sample area covered by droplets in **Figure 3**. The fraction of surface area covered by droplets greater than droplet radius r but less than droplet radius $(r + dr)$ is expressed in terms of Equation 2.9 by means of a first-order, forward Taylor series expansion of f about r

$$A(r) dr = f(r) - f(r + dr) = -f'(r) dr \quad (2.10)$$

The constrained surface area fraction $A(r)$ is just the product of projected droplet area a with the number of droplets per unit area N of the condensing surface between r and $(r + dr)$

$$A(r) dr = a(r)N(r) dr = \pi r^2 N(r) dr \quad (2.11)$$

The projected droplet area must be specified because the radius r is defined as the radius of the spherical droplet cap, not of the circular contact area between droplet and surface. This is chosen

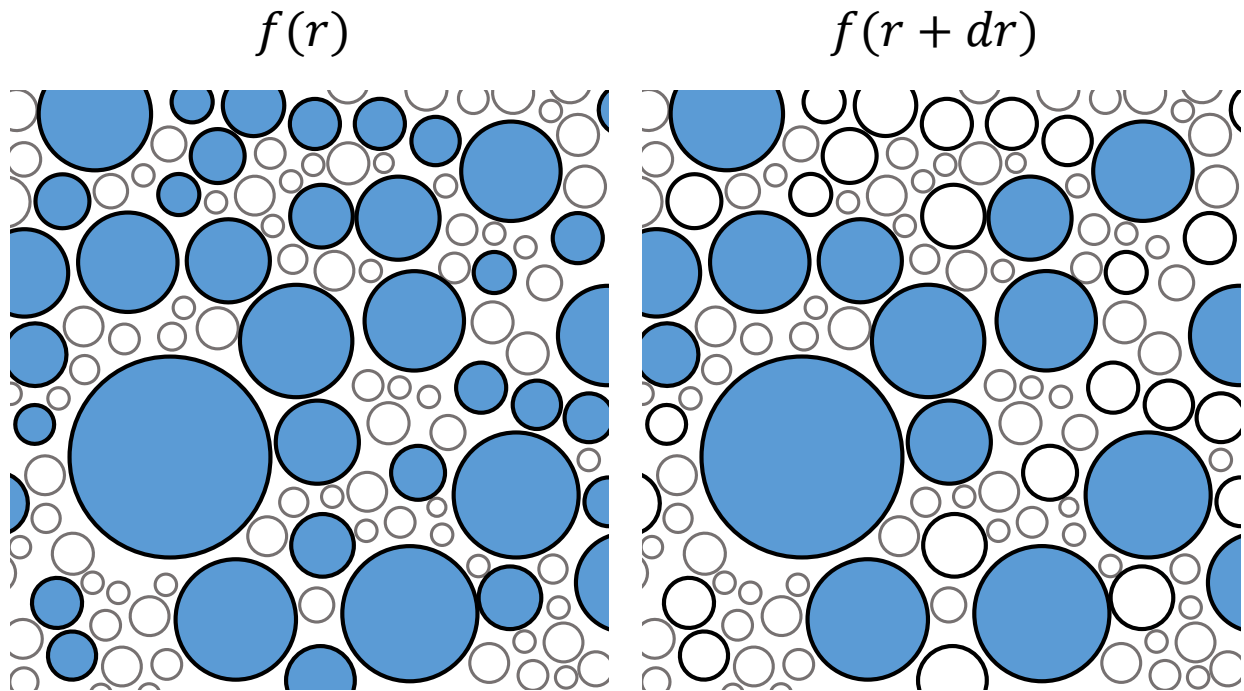
because for contact angles greater than 90° , optical measurement of droplet radii normal to the surface yields the spherical cap radius, not the circular base radius. With the radius expressed this way, the model neglects droplets that form under the canopy of other, larger droplets.

Combining Equations 2.9 – 2.11 yields LeFevre and Rose's model [2] of the droplet size distribution with a variable b index

$$N(r) = \frac{b}{\pi r^3} \left(\frac{r}{r_{max}} \right)^b \quad (2.12)$$

which gives the number of droplet counts expected between radii r and $(r + dr)$ per unit area of the condensing surface. LeFevre and Rose chose a value of $1/3$ for the b index. Rose clarifies in a later paper that $1/3$ was chosen for this index to best fit the data available at the time [24].

Results were subsequently verified by Graham [25] and by Rose and Glicksman [26]. The index is left unexpressed so that it can vary in a nonlinear fit of experimental data to the theoretical form of the droplet size distribution.



$$A(r) dr = f(r) - f(r + dr)$$

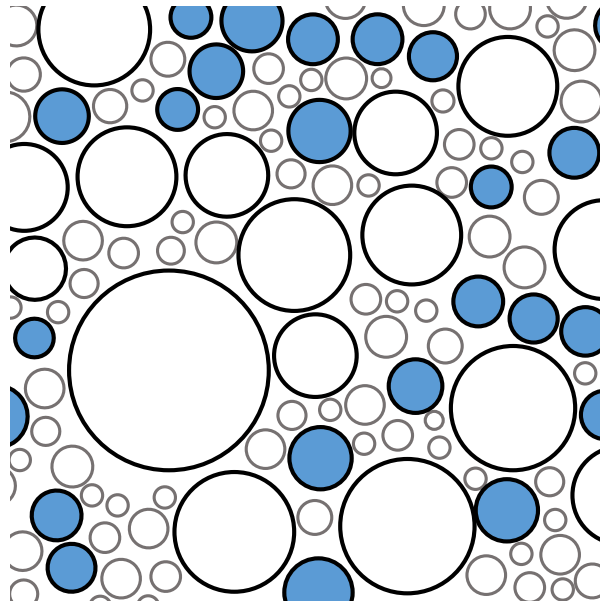


Figure 3. Representation of Area Fractions

Top-left: Fractional area $f(r)$ covered by droplets with radius greater than r .

Top-right: Fractional area $f(r + dr)$ covered by droplets with radius greater than $(r + dr)$.

Bottom: Fractional area $A(r) dr$ covered by droplets with radii between r and $(r + dr)$.

2.3. Small Droplet Size Distribution

The droplet size distribution presented in Equation 2.12 is based on the assumptions that direct condensation occurs at droplet caps and that neighboring droplets coalesce when they overlap. This is accurate for large droplets. However, coalescence does not occur for droplets with a radius smaller than the nucleation site density. The droplet size distribution is overpredicted below the critical radius. Models of the small droplet size distribution have been proposed [2,23,27,36]. The specific model presented here is the one proposed by Kim and Kim [23]. The critical radius below which the small droplet distribution takes over is defined

$$r_e = (4N_s)^{-1/2} \quad (2.13)$$

where N_s is the condensing surface nucleation site density and nucleation sites are arranged in a square grid. The nucleation site density is $2.5 \times 10^{11} \text{ m}^{-2}$ from the literature [23]. This model accounts for growth of droplets by direct deposition and surface renewal due to sweeping of large droplets. The surface renewal rate S is related to the sweeping period

$$\tau = \frac{A_s}{S} \quad (2.14)$$

where A_s is the area of the condensing surface being considered. The surface renewal rate is the area of surface swept by departing droplets per unit time. The sweeping period is the time taken for the entire surface to be swept. The small droplet distribution n by Kim and Kim [23] is made consistent with the large droplet size distribution by boundary conditions at the equivalent radius r_e such that

$$n(r_e) = N(r_e) \quad (2.15)$$

$$\frac{n'(r_e)}{n(r_e)} = \frac{N'(r_e)}{N(r_e)} \quad (2.16)$$

where n is the small droplet size distribution and n' is its derivative with respect to radius, and N is the large droplet size distribution and N' is its derivative. The first condition states that both distributions must be equal at the equivalent radius. The second condition states that the logarithmic derivative with respect to r must be equal at the equivalent radius. The latter is imposed because the large droplet size distribution is linear in log-log scale, and the log slope of the small droplet distribution should match at the equivalent radius.

The boundary conditions were solved for a b index of 1/3 by Kim and Kim [23].

Therefore, the resulting small droplet size distribution in their paper is dependent upon a b index of 1/3. Since a nonlinear least-squares fit to experimental data with arbitrary b index is desired, the general form of the small droplet size distribution is obtained here

$$n(r) = N(r_e) \frac{r}{r_e} \frac{r_e - r_{min}}{r - r_{min}} \frac{A_2 r + A_3}{A_2 r_e + A_3} e^{B_1 + B_2} \quad (2.17)$$

where

$$A_1 = \frac{\Delta T}{2\rho H_{fg}} \quad (2.18)$$

$$A_2 = \frac{\theta(1 - \cos \theta)}{4k_c \sin \theta} \quad (2.19)$$

$$A_3 = \frac{1}{2h_i} + \frac{\delta(1 - \cos \theta)}{k_{coat} \sin^2 \theta} \quad (2.20)$$

and

$$B_1 = \frac{A_2}{\tau A_1} \left[\frac{r_e^2 - r^2}{2} + r_{min}(r_e - r) - r_{min}^2 \ln \left(\frac{r - r_{min}}{r_e - r_{min}} \right) \right] \quad (2.21)$$

$$B_2 = \frac{A_3}{\tau A_1} \left[r_e - r - r_{min} \ln \left(\frac{r - r_{min}}{r_e - r_{min}} \right) \right] \quad (2.22)$$

where ΔT is the subcool temperature, ρ is the density of condensate, H_{fg} is the enthalpy of vaporization of condensate, θ is the water contact angle, k_c is the coating thermal conductivity, h_i is the liquid-vapor interfacial heat transfer coefficient, δ is the coating thickness, and k_{coat} is the coating thermal conductivity. By inspection, Equation 2.17 and Equation 2.12 are equal when r is set to r_e , satisfying the first boundary condition in Equation 2.15. The logarithmic derivative boundary condition in Equation 2.16 pertains to the unknown sweeping period τ . It can be shown that Equation 2.16 is independent of the b index, and as such, the sweeping period τ is independent of the b index as well

$$\tau = \frac{3r_e^2(A_2r_e + A_3)^2}{A_1(11A_2r_e^2 - 14A_2r_er_{min} + 8A_3r_e - 11A_3r_{min})} \quad (2.23)$$

The combined droplet size distribution accounts for direct growth of small droplets, direct growth and coalescence of large droplets, as well as periodic sweeping by the largest droplets.

2.4. Heat Flux and Equivalent Heat Transfer Coefficient

Heat flux through the surface is obtained by combining the previously obtained droplet distribution with the heat transfer through a single droplet in Equation 2.7. The model of heat flux and an equivalent heat transfer coefficient is obtained as follows

$$q'' = \int_{r_{min}}^{r_e} q_d n dr + \int_{r_e}^{r_{max}} q_d N dr \quad (2.24)$$

$$h_{eq} = \frac{q''}{\Delta T} \quad (2.25)$$

where the first integral represents the heat flux due to small droplets and the second integral represents the heat flux due to large droplets. Small droplets are represented by the small droplet distribution n that ranges from the minimum thermodynamically viable droplet radius r_{min} to the

radius at which coalescence begins r_e . Large droplets are represented by the large droplet distribution N which ranges from r_e to the departing droplet radius r_{max} . This heat flux considers only the effect of the coating and condensate layer. This defines the maximum heat flux possible for a given implementation of the coating. The equivalent heat transfer coefficient lumps the coating and condensate into a single, equivalent convection term. This term accounts for the effect of the coating and condensation characteristic on the surface, and varies with the assumed or measured subcool temperature. This can be used in the comparison of different surface treatments, although in this study the surface treatment is consistent across samples. In a real implementation, the heat flux depends on additional thermal resistances beneath the coating. This is considered when comparisons are made to measurements of heat flux on a plate and tube surface.

Chapter 3. Experimental Setup

Two apparatuses are used to explore condensation on the plate and tube geometry. The Plate Condensing Heat EXchanger (PC-HEX) has been built as a part of this study, while the Tube Condensing Heat EXchanger (TC-HEX) apparatus was developed in a previous study [30]. The PC-HEX and TC-HEX apparatuses feature external condensation on a plate and tube geometry, respectively. The convenient surface geometry in the PC-HEX apparatus facilitates condensate visualization, from which heat flux is estimated. These results are compared with those from the TC-HEX apparatus.

3.1. Plate Condensing Heat Exchanger (PC-HEX)

The PC-HEX apparatus consists of a central pipe cross with four interchangeable flange ends. One flange end is dedicated to each of the following tasks: sample mounting and cooling, boiling water, condensate measurement, and ambient condition monitoring and control. Details of the apparatus, installed instrumentation, and the experimental method used are described here.

3.1.1. Apparatus

The PC-HEX apparatus is designed for optimal condensate visualization and ease of assembly. The apparatus consists of an enclosed chamber with a large viewport opposite the flat plate sample, a boiler, and pressure and temperature sensors. The chamber is mounted to a strut channel frame. A solid model rendering of the design intent is portrayed in **Figure 4**. The core of the chamber is a four-way pipe cross with an internal diameter of 102 mm. Flange connections are welded to the four legs of the chamber, allowing for mounting of flange caps. Compressible gaskets are used at the mating surface of flanges and flange caps. The following figures depict the chamber in its uninsulated state for clarity of function. The final state of the chamber also includes insulation, as is seen in **Figure 9**.

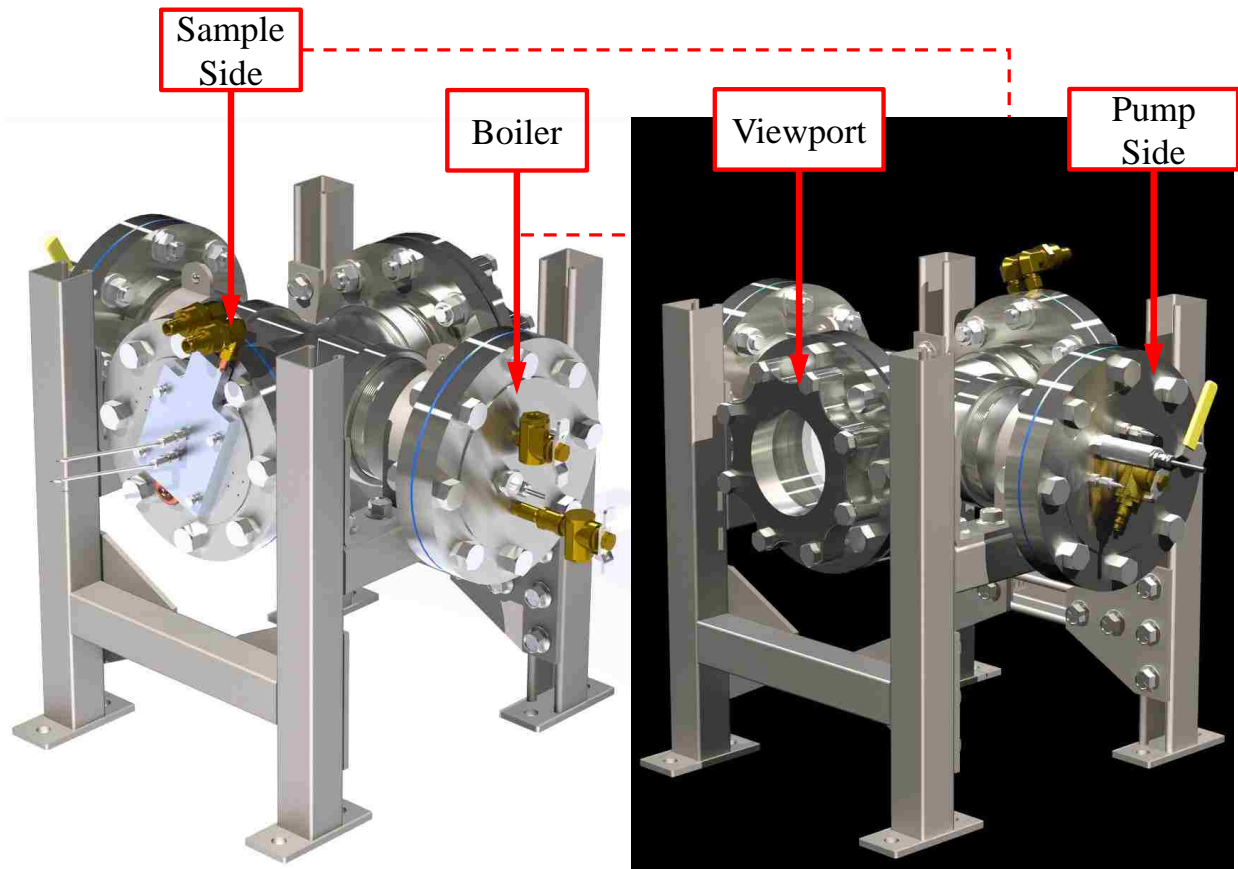


Figure 4. PC-HEX Design Render

The chamber features four flange caps with unique capabilities. A flat plate sample is mounted and cooled on the sample side. Another flange features an internal boiler and condensate drain. A borosilicate viewport is bolted to the third. The fourth flange houses sensors and a pump valve.

The sample side flange is pictured in **Figure 5**. A flat plate is mounted to a copper plug, which is installed in the chamber and backed by the cold plate. Coolant circulates at 150 g/s through a U-shaped copper tube (with 8 mm ID) inside the aluminum cold plate. A process chiller is used to supply the coolant. Two T-type thermocouples are embedded in the copper plug, just 3.2 mm from the mounted sample. The gap between flange cap and plug is sealed by two O-rings. The flat plate sample is mounted to the plug by two screws. The viewport is mounted opposite the sample side flange to permit viewing of condensate on the sample.

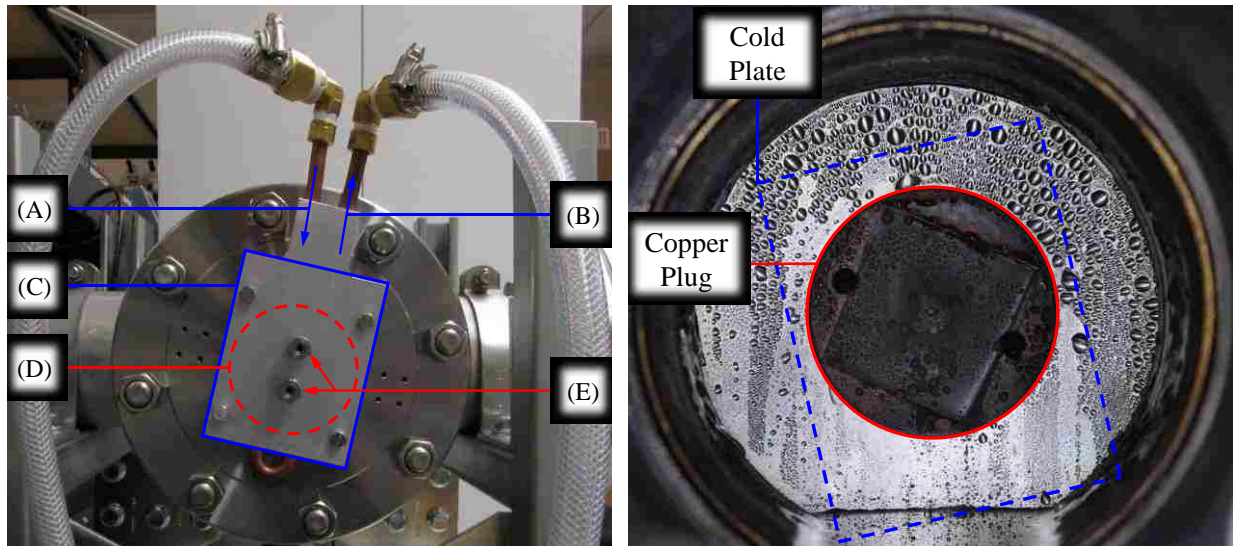


Figure 5. PC-HEX Sample Side Flange

Left: The sample side flange exterior. (A) Coolant in. (B) Coolant out. (C) Cold plate. (D) Copper plug. (E) Thermocouple ports. *Right:* The interior as seen from the viewport flange. The sample is mounted to the copper plug.

The copper plug is also shown in **Figure 6**, where the canopy is seen more clearly. The plug is placed in the apparatus such that the canopy shields the plate from condensate runoff from above. Thermal paste is applied between the sample and copper plug to ensure good thermal contact. The sample has a PTFE-based hydrophobic coating and is supplied by a confidential industry contact. Small tapped holes on the back of the plug permit affixing a handle to the plug for easy installation and removal from the chamber. The cold plate is tightened against the back of the plug, compressing the face-sealing O-ring and ensuring good thermal contact. Thermal paste is also applied at the interface between the cold plate and plug.

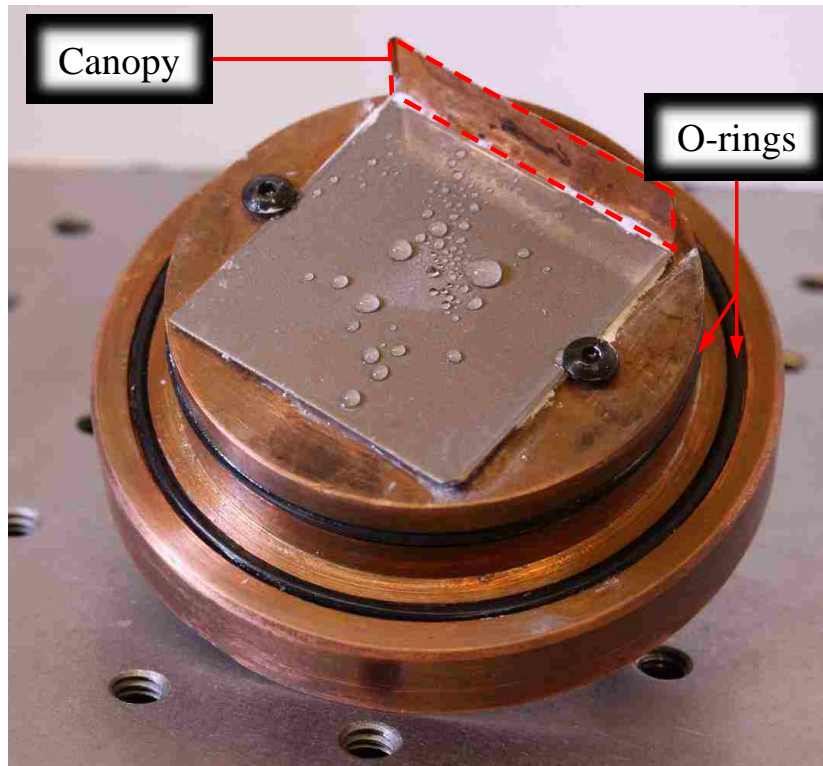


Figure 6. PC-HEX Sample Mounted to Copper Plug

The copper plug is installed in the sample side flange cap and seals with two O-rings. A canopy is installed above the sample to prevent condensate runoff from above the sample affecting the results. The sample is weatherable PTFE-based coating supplied by a confidential industry contact.

The boiler flange is pictured in **Figure 7**. A 250 W cartridge heater is installed in a 500 cm³ internal boiler. This volume is measured from just below the steam outlet and just above the cartridge heater. At the heating rate supplied, the boiler is sized to supply steam for over an hour. The floating ball bearing in the sight gauge sinks when the boiler water level drops too low, indicating the need to refill the boiler. The fill valve is used to fill the boiler. The drain valve is used to remove condensate from the main chamber. The drain is installed in the 10 cm of annular space between the concentric 73 mm OD boiler and 102 mm ID chamber. An outlet on the far end of the boiler permits steam into the main chamber, where it condenses on the sample as well as the walls of the chamber. Auxiliary heating pads and insulation limit most of the condensation to the sample side wall.

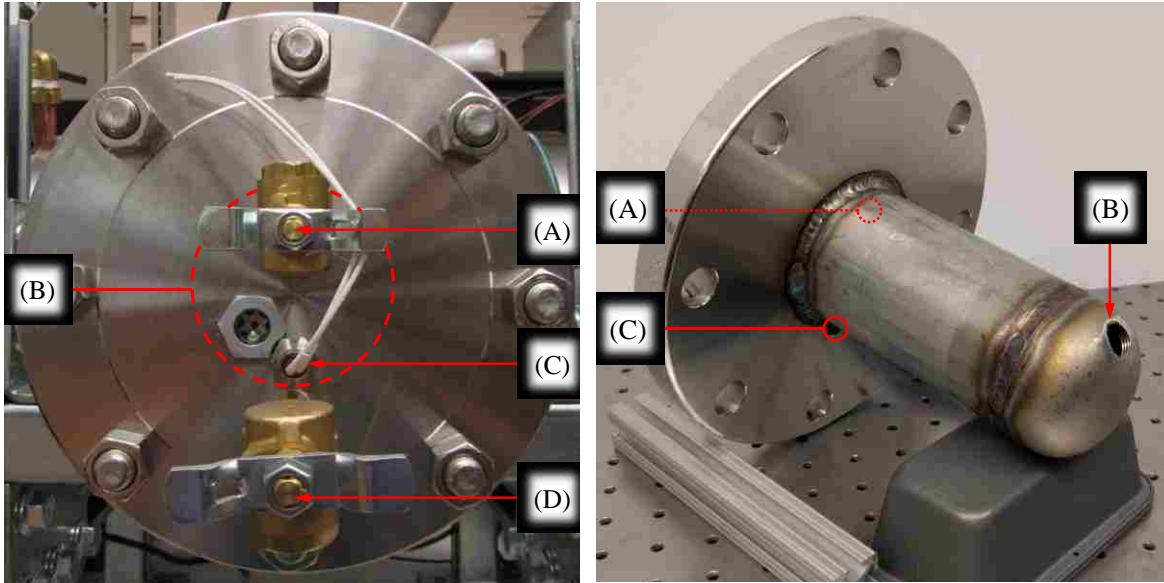


Figure 7. PC-HEX Boiler Flange

Left: The boiler flange exterior. The boiler holds roughly 500 cm^3 of water. (A) Boiler fill valve. (B) Outline of internal, concentric boiler. (C) A 250 W cartridge heater. (D) Condensate drain valve. *Right:* The internal boiler, which is a butt-welded tube with an outer diameter of 73 mm is concentric with the chamber. (A) The boiler fill valve leads to the boiler. (B) Steam outlet to the chamber. (C) The condensate drain valve leads to the bottom of the chamber.

3.1.1. Handling of Noncondensable Gases

The pump side flange is shown in **Figure 8**. A pressure transducer and two T-type thermocouples are used to monitor ambient conditions. Noncondensable gases in air hinder condensation and reduce the effective nucleation density of surfaces inside the chamber. It is desired to remove as much air from the chamber as possible, so a pump valve has been installed. Data regarding the expected leak rate of the chamber is shown in **Appendix A**. The conditions measured by the pump side flange are far enough from the cold plate to assume accurate readings of the ambient saturation temperature and pressure. The assembled PC-HEX apparatus is shown in **Figure 9**. Auxiliary heating pads and insulation is installed to reduce start-up time and offset heat loss to the significant mass of the chamber. The compactness of the resulting design is convenient for visualization of condensation with a modest focal length lens. The flange cap design is also modular, allowing re-design and replacement of individual components.

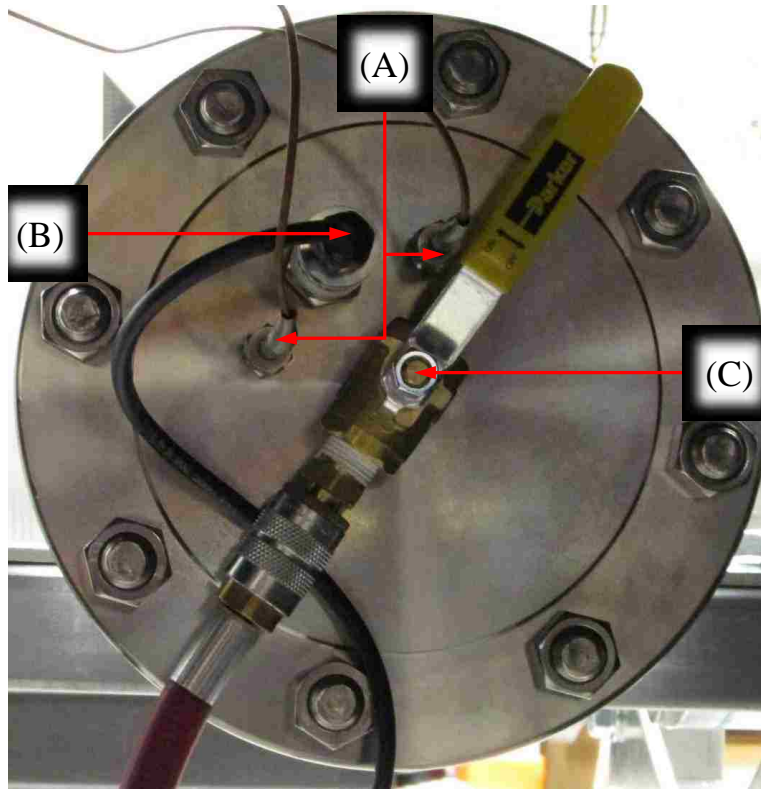


Figure 8. PC-HEX Pump Side Flange

The pump side of the system, with sensors and a pump valve. (A) Thermocouples. (B) Pressure transducer. (C) Pump valve.

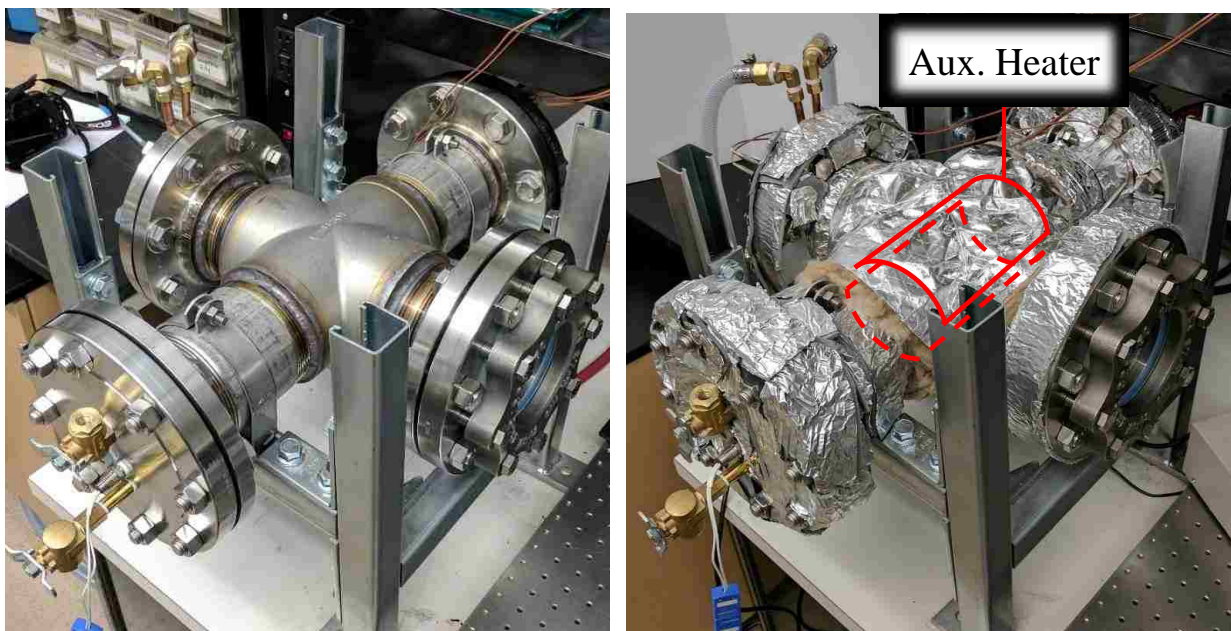


Figure 9. PC-HEX Apparatus

Left: The state of the chamber prior to installation of the auxiliary heater and insulation.
Right: Auxiliary heating pads are installed between the chamber and insulation.

3.1.2. Experimental Method

The purpose of the PC-HEX apparatus is to visualize condensate on a flat plate. Video data is processed for droplet detections. These detections make up the measured droplet size distribution in each frame of video data. The experimental method outlined here has been designed to maximize the consistency of optical condensate measurement. What follows is a description of the setup procedure for active components and data acquisition, camera setup, as well as start-up and runtime procedures.

Active components in the design include the pump, chiller and boiler, and auxiliary heating pads. The pump is used to achieve a rough vacuum of about 14 kPa absolute pressure in the chamber. The chiller consists of two closed loops, one of which is supplied by facility water, and the other which circulates deionized water through the cold plate. A PID temperature controller is used to control heat output from the auxiliary heating pads, which are affixed to the outside of the pipe cross. The temperature input is a thermocouple contacting the outside surface of the pipe cross. The power source for the pads is controlled by the temperature controller.

There are four T-type thermocouples and a pressure transducer installed in the apparatus. A National Instruments DAQ is used in conjunction with LabVIEW to obtain sensor readings. The LabVIEW block diagram made for this purpose is shown in **Figure 10**. The thermocouples have been calibrated at the temperatures of an ice bath and boiling water. Two thermocouples each monitor plate temperature and ambient temperature. The PX309-030AV absolute pressure transducer has a linear characteristic established by the 5-point NIST certificate provided by the manufacturer. The pressure transducer monitors ambient pressure. Readings are captured alongside the current system time, which is synchronized with the system time for the cameras used in the experiment.

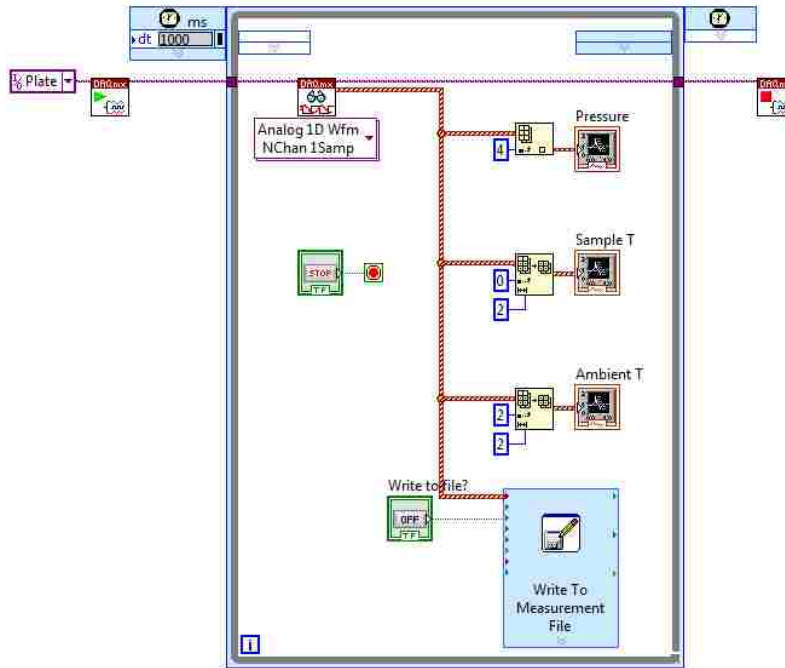


Figure 10. LabVIEW Block Diagram for PC-HEX Data Acquisition

The block diagram used to acquire temperatures and pressures in the PC-HEX apparatus.

The camera is mounted on an optical bench by clamps and an adjustable post. A cinema lens with 135 mm fixed focal length is used with two different cameras in this setup. One of the cameras used is a high-speed camera capable of 3.6 Gbit/s throughput and 2 GB memory. The maximum square resolution of 600×600 pixels yields as much as 1300 fps recorded over 4 s. However, a balance between speed, single capture duration, and lighting governs the decision to capture footage at 360 fps for about 15 s. A photo of this setup is shown in **Figure 11**. While the high-speed camera is appropriate for capturing short-lived condensation sweeping events, a Digital Single-Lens Reflex (DSLR) camera is employed to obtain continuous recording of long term condensate patterns. At a resolution of 720×720 pixels and 60 fps, the DSLR yields detections of smaller droplets at the expense of framerate. In both cases, an LED ring light is affixed to the viewport to illuminate the sample. Minimizing the distance between the light and the window reduces glare.

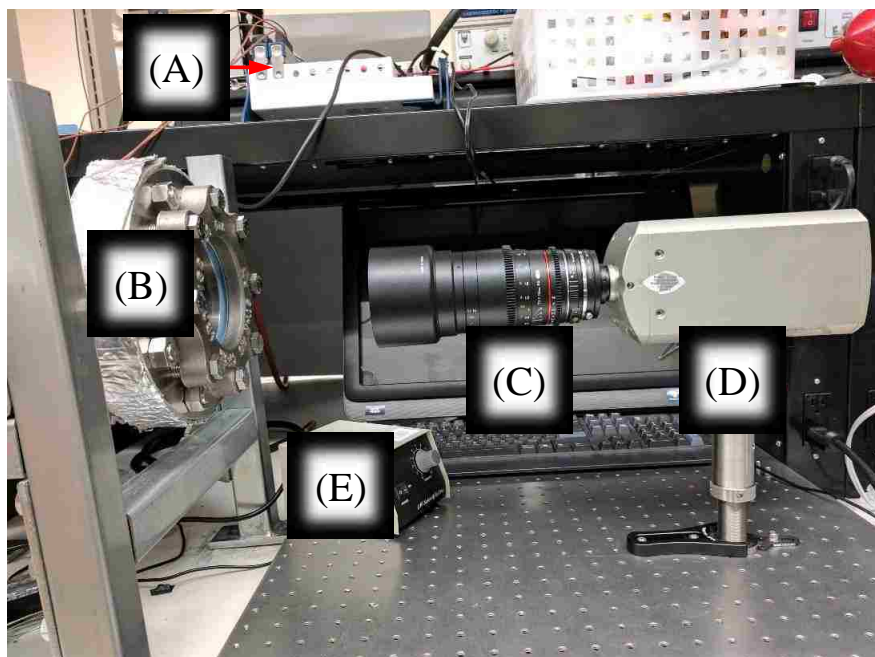


Figure 11. PC-HEX High-Speed Camera and Data Acquisition Setup

(A) Data acquisition device. (B) Viewport of PC-HEX. (C) The lens has a focal length of 135 mm. (D) High-speed camera. Resolution of 600×600 pixels and up to 1000 fps. (E) Ring light controller.

System start-up begins with opening all valves and removing the copper plug from the chamber. A temporary handle is installed on the exterior side of the plug to unseat it from the sample side flange cap. Thermal paste is applied and the sample is mounted using the internal screws. The plug is re-inserted and its handle is removed. The cold plate is mounted, with thermal paste applied between it and the copper plug. The boiler is refilled and any condensate left in the chamber is removed, after which the boiler side valves are closed. A preliminary video is captured of the bare plate sample to obtain lighting characteristics. This is used later to equalize illumination on the sample and remove background imperfections, if necessary. The pump side valve is opened and air is pumped out of the chamber. Once sensor readings indicate negligible change in pressure with time, the valve is closed and the pump turned off. At this point, the boiler is turned on, auxiliary heating pads are set to the desired temperature, and the coolant inlet temperature is set.

Runtime procedures begin when chamber pressure has reached at least 60 kPa. The chiller temperature is reduced to obtain the desired subcool temperature. Condensation begins to generate on the sample surface. Video is captured when subcool temperature stabilizes and sufficient cycles of condensation growth and sweeping have passed. The viewport must be defogged by use of a heat gun, permitting at least fifteen minutes for video capture before it must be defogged again. This process is repeated as needed to capture video at different subcool temperatures. The boiler must be periodically refilled, and it is encouraged, but not necessary, to drain the condensate pool in the chamber whenever the boiler is refilled. This cuts down on glare from reflections off the condensate water level below the sample. Vacuum must be pulled in the chamber again whenever the boiler is refilled.

When the experiment is complete, the chiller is set to room temperature and the boiler and heating pads are turned off. Condensate is drained and the cooldown process begins. Runtime data is presented in **Appendix A** for the samples used in this study.

3.2. Tube Condensing Heat Exchanger (TC-HEX)

The core of the TC-HEX apparatus is a horizontal tube sample section mounted in a condenser. Coolant flows inside the tube sample, while condensate forms on the outer wall of the tube. A boiler is required to supply steam to the condenser. Details of the apparatus, installed instrumentation, and the experimental method used are described here.

3.2.1. Apparatus

The TC-HEX apparatus is designed for measurement of the heat flux through a horizontal tube sample. The boiler and condenser are the main components. A photo of the chamber is shown in **Figure 12**. The process diagram of the chamber is shown in **Figure 13**. Some insulation has been removed for demonstration purposes. A pump valve permits the removal of

air from the apparatus prior to experimentation. Facility water is connected to a temperature-controlled loop that circulates water through a coil inside the boiler chamber of the TC-HEX apparatus. A pool of deionized water in contact with the coil boils and follows the steam path above the chamber. Steam flows into the condenser where it condenses onto the outer wall of the cooled tube sample. Condensate then returns to the boiler by a return path below the condenser. Condensation occurs elsewhere in the apparatus as well, but heat losses are minimized by a bed of loose-fill insulation around each chamber, as well as insulation along the steam path and condensate return.

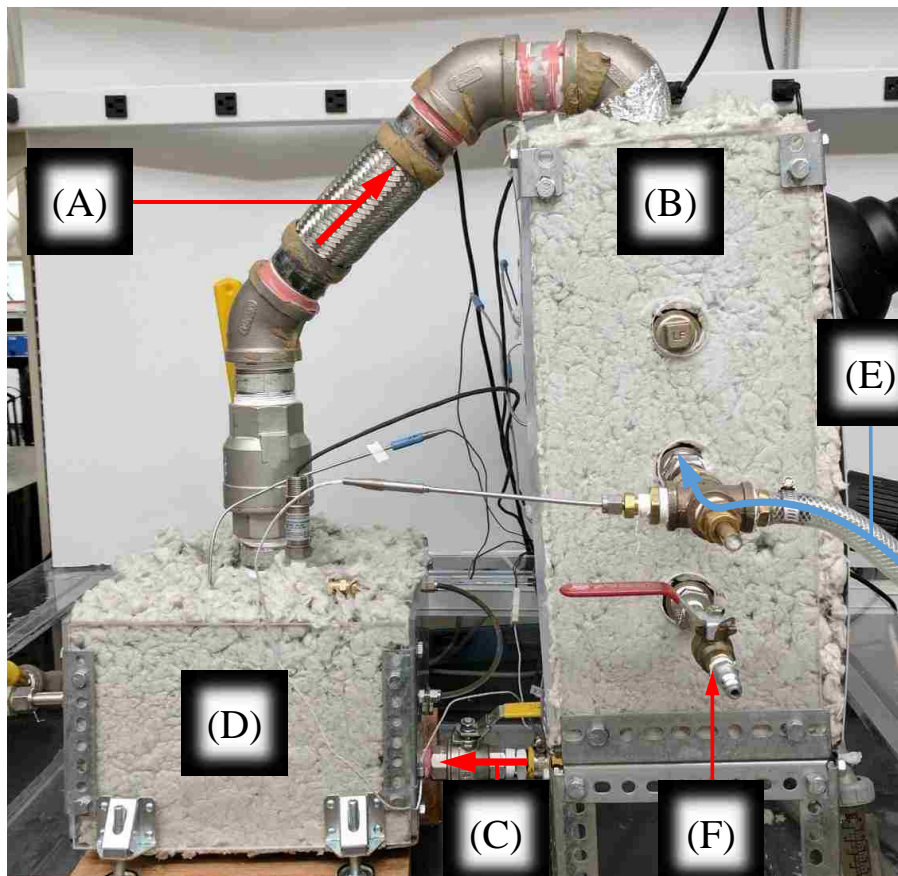


Figure 12. TC-HEX Apparatus

Steam travels up the steam path (A) into the condenser (B). Steam condenses on the tube, which has internal coolant flow (E). Condensate flows along the return line (C) back to the boiler (D), which provides steam to the steam path. The vacuum pump valve (F) is used to remove air from the chamber.

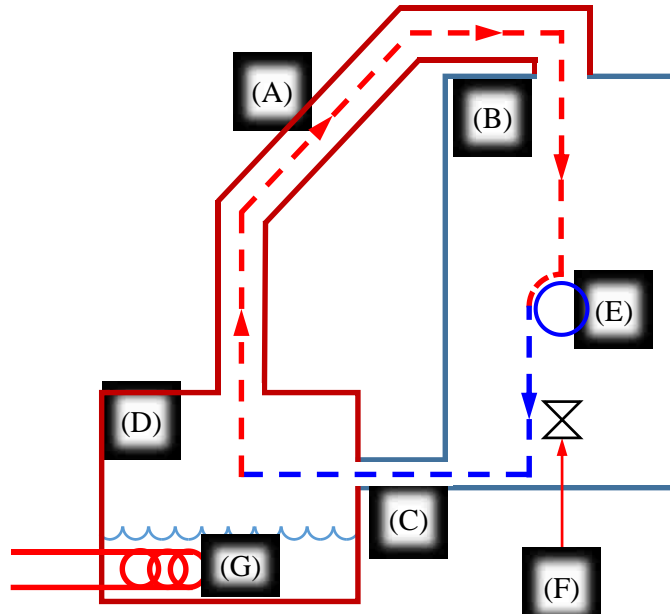


Figure 13. TC-HEX Process Diagram

Steam travels up the steam path (A) into the condenser (B). Steam condenses on the tube, which has internal coolant flow (E). Condensate flows along the return line (C) back to the boiler (D), which provides steam to the steam path. Boiler water is heated by a temperature-controlled loop (G). The vacuum pump valve (F) is used to remove air from the chamber.

The tube sample is cooled by a deionized water loop from the chiller. The chiller circulates 150 g/s of water through the tube. A top-down view of the inlet to the tube is shown in **Figure 14**. The inlet and outlet fixtures are at the front and rear of the condenser, respectively, and feature the same design. The treated sample is mounted to the chamber with compression fittings at the front and rear. A brass pipe cross is fitted onto the end of the sample with another compression fitting. A coolant inlet and resistance temperature detector (RTD) mount are mounted to the pipe cross perpendicular to the tube sample. There is an RTD at both the coolant inlet and outlet. A brass inner tube is inserted into the sample, fitted at the far end of the pipe cross, creating an annular space for coolant to flow. The annular cross-section, pictured in **Figure 25**, reduces the required flow rate to achieve adequate cooling and ensures a more uniform coolant temperature profile. The inner tube contains air, but is capped with loose fill insulation to prevent unintended heat loss.

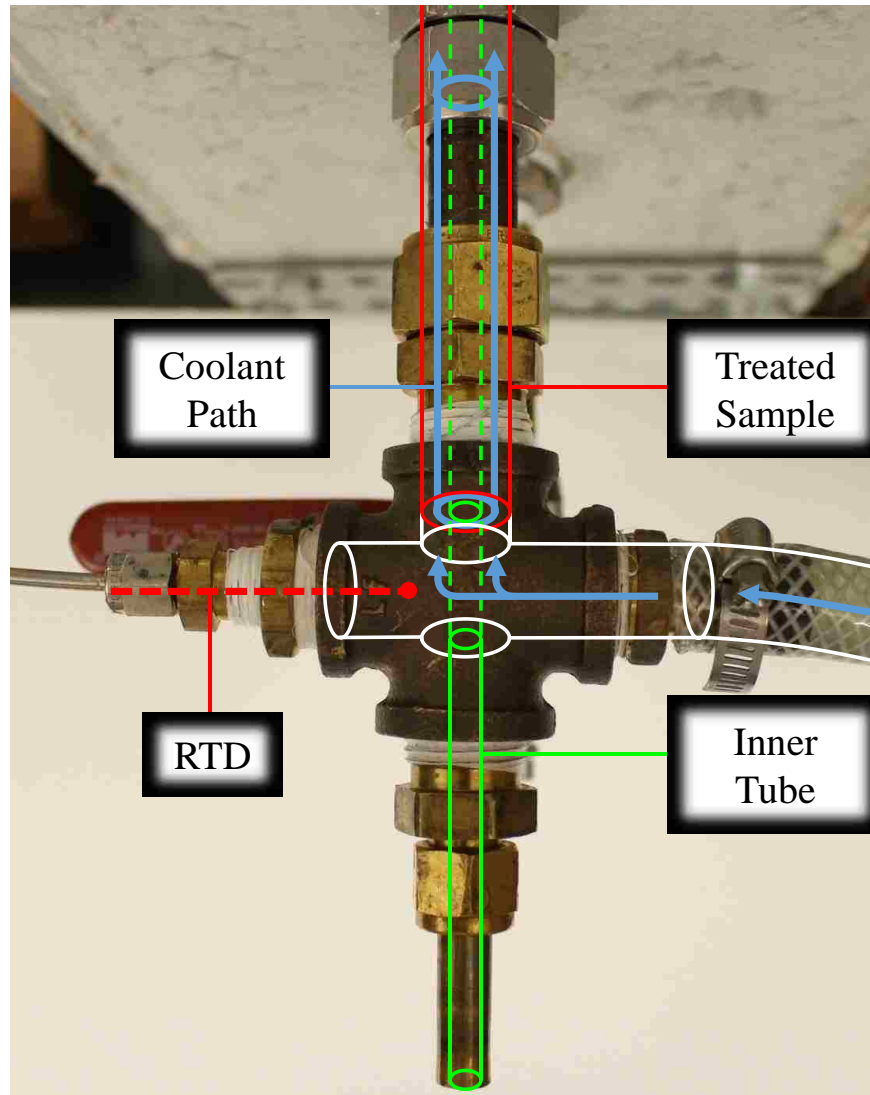


Figure 14. TC-HEX Inlet Coolant Line

The pipe cross has four connections. It is mounted to the sample tube at the top, the inner tube at the bottom, and features an RTD and coolant inlet to the left and right, respectively. Coolant flows in the annular space between the inner and outer tubes.

Instrumentation used for the TC-HEX apparatus is shown in **Figure 15**. Five T-type thermocouples and two pressure transducers monitor ambient conditions in the boiler and condenser. Two RTD's monitor coolant inlet and outlet temperatures. There is also a check valve on the boiler in case of overpressure. A high-speed camera is mounted outside of the central viewport to record condensation on the outside wall of the tube sample. Lighting is directed into the upper and lower viewports to illuminate the sample during recording only.

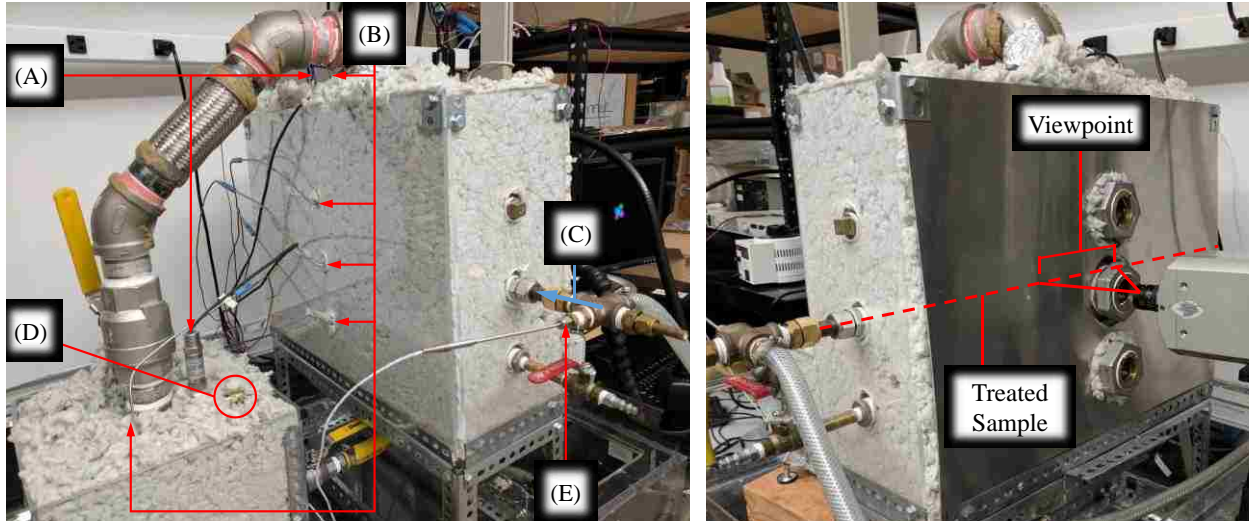


Figure 15. TC-HEX Instrumentation

Left: View of the boiler and the left side of the condenser. (A) Pressure transducers. (B) Thermocouples. (C) Coolant flow path. (D) Boiler check valve. (E) Coolant inlet RTD (coolant outlet RTD at back of apparatus). *Right:* View of the right side of the condenser. The camera and its viewpoint of the tube sample are shown.

3.2.2. Experimental Method

The TC-HEX apparatus is designed for measurement of heat flux by coolant temperature monitoring. The long tube test section maximizes the coolant temperature difference measured for a given condition. A description of the setup procedure, start-up and runtime procedures follows.

Installing the tube sample requires mounting it to the condenser, attaching the front and rear coolant lines, and installing the inner tube. All tube-to-pipe connections are made with compression fittings. The front tube-to-condenser compression fitting is removed entirely to prevent abrasion of the sample as it is slid into the condenser. The tube is then secured to the condenser at both ends. Next, coolant lines are fixed to the front and back of the tube sample. The inner tube is slid into the outer tube and mounted to the front and back coolant lines. This completes the mounting process for the tube sample.

Start-up procedures involve pumping and warmup of the boiler and chiller. The vacuum pump is attached to the pump valve by a hose and air is removed from the chamber. Pumping continues until the pressure inside the chamber is no longer changing significantly. The valve is closed and hose disconnected. The facility water lines for the boiler and chiller are then turned on. The boiler is turned on and set to 115°C. Once the chamber pressure rises above atmospheric, the boiler temperature is reduced to 105°C and the pump valve is reopened to achieve blowdown. Exiting steam and entrained air leave the chamber, further reducing the partial pressure of air in the chamber. The valve is closed and the chiller is turned on. The chiller is set to 90°C and allowed to warm up.

Runtime procedures begin once the chiller inlet and outlet temperatures are steady. Data points are taken when measured ambient and coolant conditions are steady for ten minutes or longer. The values of each thermocouple, RTD, and pressure transducer are taken for a prescribed chiller temperature. The chiller temperature is reduced by a constant increment and the process is repeated. When it is desired to capture high-speed video of the condensation process, viewports are defogged and lighting is introduced to the chamber by the top and bottom viewports. The camera records footage from the middle viewport. Afterward, the lights are turned off to prevent unintended radiative heating of the tube.

Shutdown procedures begin once enough data points have been taken for a given tube sample. The boiler and chiller temperatures are returned to room temperature, allowed to cool down, and then shut off. New samples are not fitted until cooldown is complete.

Chapter 4. Data Handling

Data captured from each apparatus is handled differently. Video data from the PC-HEX apparatus is first processed for droplet detections. Next, the droplet size distribution, heat flux, and an equivalent heat transfer coefficient are found. Uncertainty of droplet detections is also considered. Numerical measurements from the TC-HEX apparatus require less pre-processing, but the droplet size distribution is not measured. Heat flux and an equivalent heat transfer coefficient are found, and measurement uncertainty is determined.

4.1. PC-HEX Data

A modification of the original Circle Hough Transform (CHT) by Duda and Hart [37] is used to detect droplets. The method is applied to video frames that have been processed to balance illumination and remove glare. The measured droplet size distribution is obtained from droplet detections. A modification of the single droplet heat transfer model is developed to account for additional thermal resistances in the PC-HEX apparatus, and is used to estimate heat flux through the droplet population. The propagation of uncertainty from the droplet detection process is also considered.

4.1.1. Droplet Detection

Droplet detection is a specific application of general circle detection. The original CHT method employed by Duda and Hart [37] involves accumulating votes for possible centers at an estimated radius distance away from each prominent edge pixel. However, a modification of the CHT by Kimme et al. [38], as described by Davies [32], will be used instead. This method uses edge orientation to cast votes normal to the edge and in a direction dependent on the polarity of circles with respect to the background. This significantly reduces the number of votes made, and

improves the accuracy of the CHT. Additionally, a range of radii estimates may be tried in one iteration by use of the log phase coding method described by Atherton [31].

The specific implementation used in this study is a substantial modification of functions present in the MATLAB Image Processing Toolbox [39]. The code has been repurposed to be applied sequentially to different radius ranges with masking of previously detected circles. This is necessary because a wide range of circle sizes cannot be accurately detected in one pass of the CHT, but repeated passes result in duplicate erroneous detections tangent to larger circles. An example of a modified CHT, suitable for droplet detection, is performed on an image of coins on a planar surface, as seen in **Figure 16**.



Figure 16. Image of Coins and Prominent Edges

Left: An image of coins. *Right:* Candidate pixels for circle edges (shown in white) are found by computing the gradient of pixel intensities and setting an appropriate threshold below which gradients are ignored.

The first step to circle detection is establishing voters on significant image features. A Sobel operator [40] is used to compute the horizontal and vertical pixel intensity gradients g_x and g_y at each pixel, from which the gradient magnitude g is found. In the

following definition of the gradient, subscript i refers to the x-coordinate of the current pixel and subscript j refers to the y-coordinate of the current pixel

$$g_{x,i,j} = (I_{j-1} + 2I_j + I_{j+1})_{i+1} - (I_{j-1} + 2I_j + I_{j+1})_{i-1} \quad (4.1)$$

$$g_{y,i,j} = (I_{i-1} + 2I_i + I_{i+1})_{j+1} - (I_{i-1} + 2I_i + I_{i+1})_{j-1} \quad (4.2)$$

$$g_{i,j} = \sqrt{g_{x,i,j}^2 + g_{y,i,j}^2} \quad (4.3)$$

where I is the grayscale intensity at pixels specified by the indices. The Sobel operator is used because it can discern edge directions better than a simple central difference operator. An edge threshold has been chosen that removes less prominent edges, such as those of the surface beneath the coins. The resulting thresholded edges are pictured in **Figure 16**. A voter is placed at each significant edge pixel. Each voter casts a discrete number of votes at distances normal to the edge, such that

$$x_{est} = x_{voter} - r_{est} \frac{g_x}{g} \quad (4.4)$$

$$y_{est} = y_{voter} - r_{est} \frac{g_y}{g} \quad (4.5)$$

where x_{est} and y_{est} are estimates of the coordinates of a circle center with radius r_{est} and pixel subscripts i and j have been dropped. The gradient ratio in Equation 4.4 represents the cosine of the angle to the radial spoke between the voter and the estimated center, while the gradient ratio in Equation 4.5 represents the sine of the angle. The distances at which votes are cast vary between estimated radii $r_{est,min}$ and $r_{est,max}$. An example of a single voter casting votes is shown in **Figure 17**.

A phase angle ϕ is assigned to each radius estimate r_{est} between the minimum and maximum radius estimates as follows

$$\phi(r_{est}) = 2\pi \frac{\ln r_{est} - \ln r_{est,min}}{\ln r_{est,max} - \ln r_{est,min}} - \pi \quad (4.6)$$

The radius range is mapped between a phase of -180° and 180° . Vote magnitude decreases as radius increases. A magnitude M is also assigned to each radius estimate, such that the weight of the vote for estimate r_{est} varies inversely with circumference of a circle with radius r_{est} as follows

$$M(r_{est}) = \frac{1}{2\pi r_{est}} \quad (4.7)$$

This magnitude scaling is performed to even out the accumulation of votes at the centers of circles of different sizes, considering larger circles receive more voters on their circumference.

The magnitude and phase are encoded into a complex weight function w that is defined here

$$w(r_{est}) = M e^{i\phi} \quad (4.8)$$

An example of vote weights (for a radius range from 1 to 2) is shown in **Figure 17**. A single voter casts the encoded set of votes towards the center of the circle. This process is repeated for each voter. Votes that land on the same pixel are added. The vote magnitude at that pixel increases, while the phase averages. All votes from each voter are accumulated in this manner.

Once a potential circle center has been located, the value of the phase at that location decodes to an estimate of its radius. Decoding is done by inverting Equation 4.6 at the potential center pixel

$$r_{avg} = \exp\left(\ln r_{est,min} + \frac{\phi_{avg} + \pi}{2\pi} (\ln r_{est,max} - \ln r_{est,min})\right) \quad (4.9)$$

where the phase ϕ_{avg} is just the phase of accumulated votes at that pixel and r_{avg} is the decoded radius estimate.

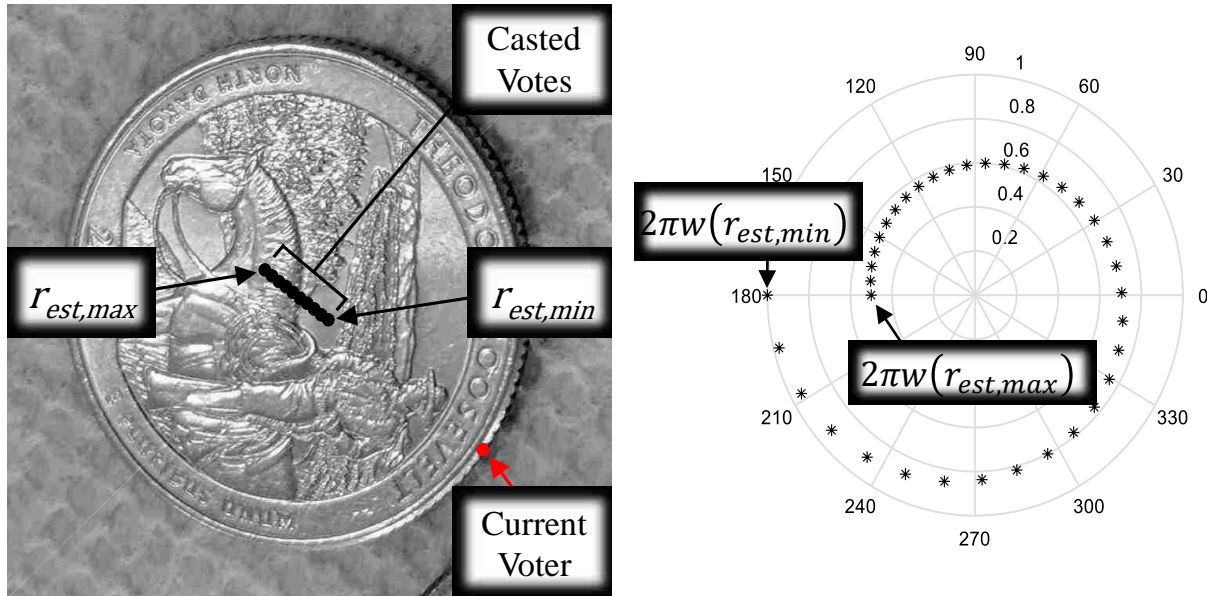


Figure 17. Examples of Single Voter and Vote Weights

Left: A single voter at an edge. The voter casts a set of votes normal to the edge. *Right:* The complex weight w given to a single voter's set of votes.

A modification of this method has been made to avoid voting outside of a specified detection region. This is useful in restraining detections to regions of active condensation on a flat plate. An example is shown in **Figure 18**. Votes only accumulate inside the yellow-outlined detection region. In the first stage, a radius range corresponding to the size of quarters is chosen.

The most significant vote accumulation occurs for votes cast towards the center of quarters. Local vote maxima below a prescribed accumulated vote threshold are hidden, after which the centroids of remaining local maxima are extracted. Centroids that fall below the accumulated vote threshold are discarded, and the remaining centroids represent detected quarters. The phase at these centroids is decoded, giving an estimate of the radius of detected quarters.

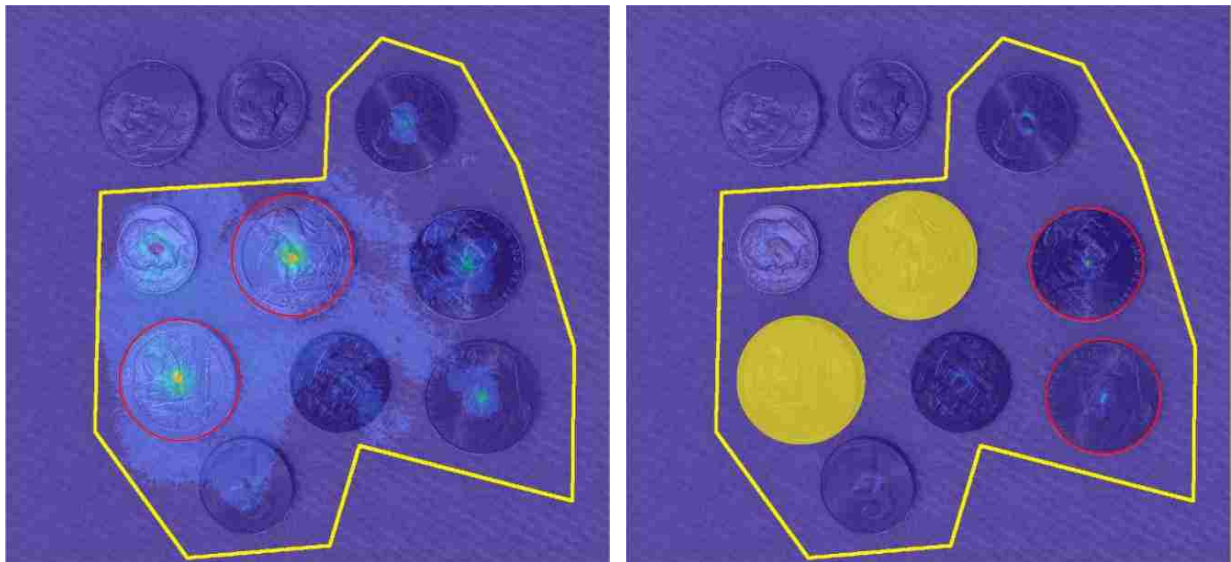


Figure 18. Quarter and Nickel Detection Stages

Left: The first detection stage. Vote accumulation is shown in a heatmap overlay. Red circles indicate positive detections in the yellow-outlined detection region. *Right:* The second detection stage. Voting is disallowed within previously detected quarters. Nickels are now detected.

This method is suitable for detecting circles over a range of radii, but votes cast will be less focused for true detections within wider ranges. This results in less accurate detection of all circles within the wider range. It is desired, then, to apply the CHT repeatedly to the same image, where the upper limit of radii to detect in any iteration is the same as the lower limit of the previous iteration. The lower limit is chosen for each iteration so that a similar number of detections occur in each iteration.

Voting on or within previously detected circles is disallowed, cutting down on voting noise in subsequent runs of the CHT. The second stage of the detection is shown in **Figure 18**. The radius range chosen focuses votes on nickels, while creating unfocused rings of accumulated votes on smaller coins. The noise present in the quarter detection stage is minimized, which was mostly due to votes cast from the arbitrary interior edges of the quarters.

The third and fourth detection stages are shown in **Figure 19**. Detection of circles with fewer edge pixels becomes more difficult, but disallowing votes within previously detected circles mitigates the issue. While the magnitude assigned to votes scales with radius, there is additional flexibility in being able to adjust the vote threshold for individual ranges. Smaller droplets also have less defined edges, requiring a lower edge threshold than with larger droplets. This detection method works best when background noise is removed in pre-processing.

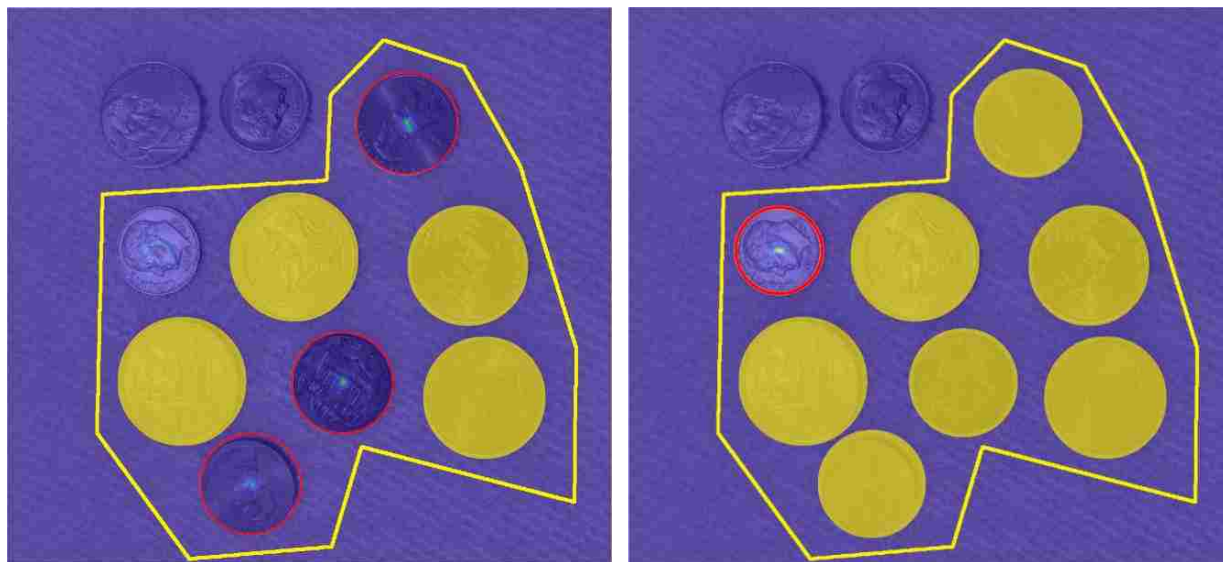


Figure 19. Penny and Dime Detection Stages

Left: The third detection stage. *Right:* The final detection stage.

4.1.2. Video Processing

Raw video is not necessarily the best input format to the droplet detection method. Uneven illumination, sample surface inconsistencies, and glare on droplets all contribute to inconsistent detections. The lighting and video capture conditions should be optimized to minimize the amount of video processing necessary, but these issues cannot be eliminated entirely. The following figures show the process on a single frame from the video data.

Background handling is carried out when illumination varies across a sample or there are local irregularities on the sample surface. The video data is pixelwise divided by an image of the background with the same illumination used during experimentation. This minimizes subtle differences in illumination and surface irregularities that affect droplet detection. An example of this process is shown in **Figure 20**. Non-destructive contrast stretching is also carried out on the resulting image to fill the range allowed by the data type. This is done linearly so that relative pixel intensities are preserved.

A detection region is established for any given input data, confining detections to just the region of the sample surface with relatively few irregularities and active condensation. The edges of a sample do not have as intimate contact with the plug and cold plate as the interior, and would artificially shift the droplet size distribution if included in the detection region. Droplet glare breaks up the circular shape of droplets and contributes noise to the detection method. Reducing droplet glare without affecting droplet edges requires morphological operations to be performed on the image. These operations are carried out in **Figure 21**.

First, a contrast stretching step is performed that tends to flatten the intensities of glare points in the image. This ensures that the following steps will affect most glare points evenly. The next step is to morphologically erode the image, eliminating droplet glare but softening

droplet edges. Finally, morphological reconstruction is performed with the contrast-adjusted image as the mask and the eroded image as the marker. This preserves edges present in the mask while taking pixel intensities from the marker. The resulting image is a good candidate for droplet detection. An example of this same image with a four-stage CHT is shown in **Figure 22**. The first stage looks for the largest droplets on the plate, with detections marked in red. Subsequent stages look for smaller droplets each time, with detections marked in green, blue, and yellow for decreasing radius. Each radius range shares its upper bound with the lower bound of the radius range above it. Video data of dropwise condensation with overlaid detections is presented in **Appendix B**.

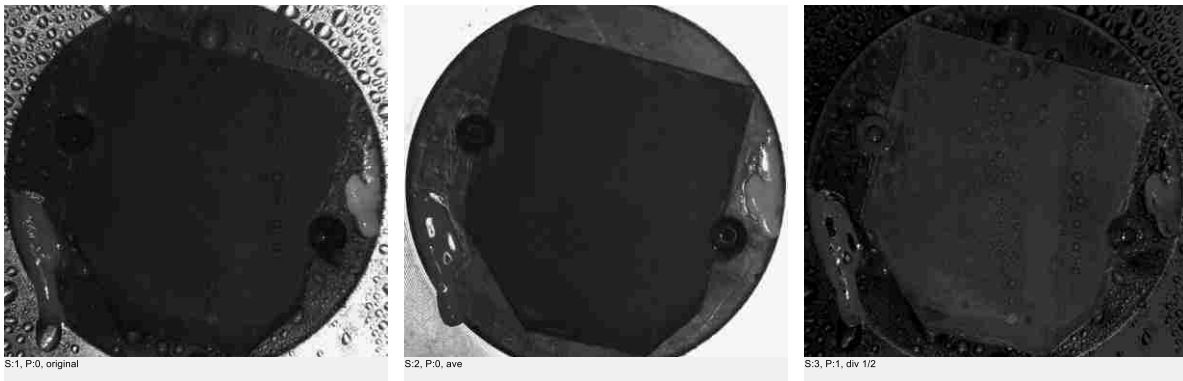


Figure 20. Background Handling Process

Left: Raw input image. *Middle:* Image of plate background with no condensate present.

Right: Result of pixelwise division of the *left* image by the *middle* image after contrast stretching.

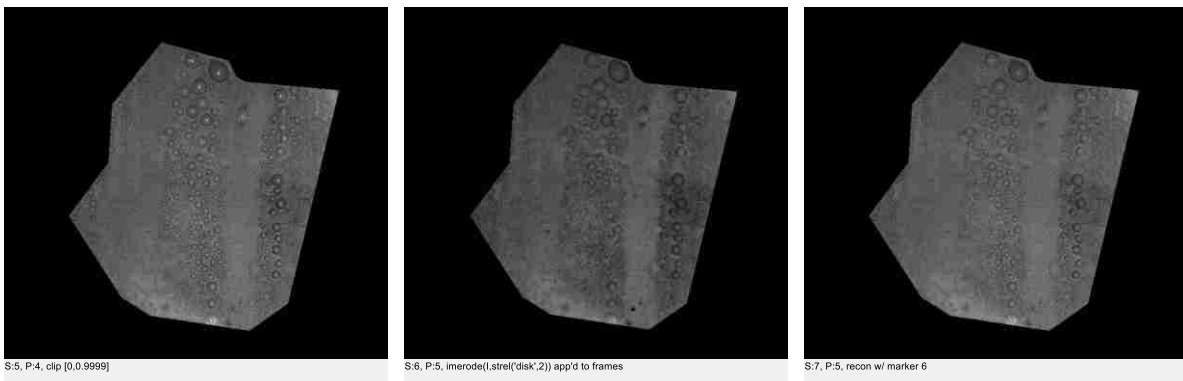


Figure 21. Detection Region and Glare Removal Process

Left: Region-restricted and further contrast-adjusted image. *Middle:* Morphologically eroded

image. *Right:* Morphological reconstruction with the *left* image as a mask and the *middle* image as the marker.

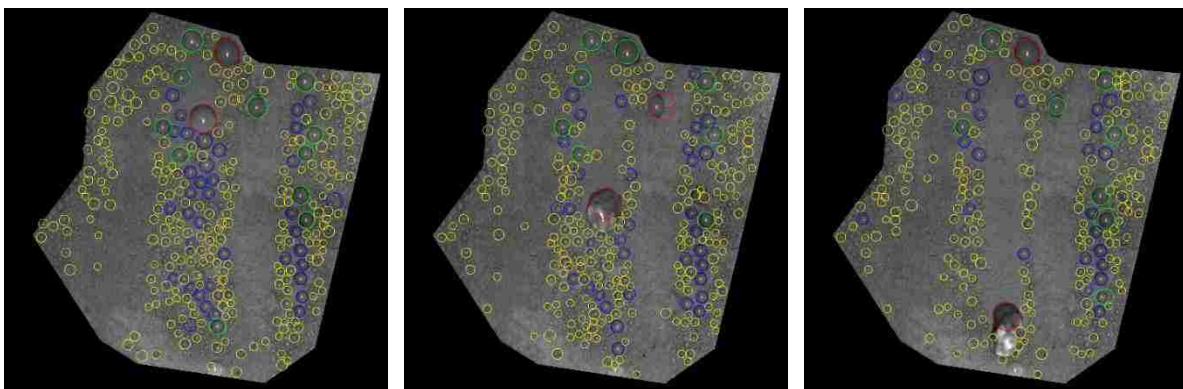


Figure 22. Droplet Detections during Droplet Sweeping Event

Detections are color-coded by the stage in which they were identified. *Left:* Video frame just

before a droplet sweeping event. *Middle:* Video frame during the event. *Right:* Video frame at the end of the event.

4.1.3. Relating Measurements to Theory

The measured droplet size distribution is found as a histogram of droplet radii with bin width Δr . The theoretical distributions N in Equation 2.12 and n in Equation 2.17 give the number of droplets per unit area per unit bin width Δr . Therefore, the theoretical distributions are presented as $N\Delta r$ and $n\Delta r$. A nonlinear least-squares fit is made of the measured distribution to the function $N\Delta r$, with variable b index. The best-fit b index is b_{mod} , informing modified distributions $N_{mod}\Delta r$ and $n_{mod}\Delta r$ which are also presented alongside the measured distribution.

Applying the theoretical model of temperature drops in the experimental setup requires measuring the saturation temperature far from the sample as well as the temperature just beneath the coating. This surface temperature cannot be directly measured in the apparatus used in this study to characterize condensation on a flat plate. Additional temperature drops are introduced to relate the actual measured temperature to the surface temperature in the model. The model describing the experimental setup is shown in **Figure 23**. The wall temperature T_w is directly measured by a thermocouple embedded in the wall near the sample. The overall temperature drop from saturation temperature T_{sat} to the chamber wall temperature T_w is

$$\Delta T_{mod} = \Delta T + \Delta T_p + \Delta T_w = T_{sat} - T_w \quad (4.10)$$

with subcool temperature ΔT defined in Equation 2.1 with $q_{d,mod}$ in place of q_d , temperature drop through the plate ΔT_p , and temperature drop through the chamber wall ΔT_w . The newly introduced temperature drops are defined for a single droplet as

$$\Delta T_p = \frac{q_{d,mod} t}{k \pi r^2 \sin^2 \theta} \quad (4.11)$$

$$\Delta T_w = \frac{q_{d,mod} t_w}{k_w \pi r^2 \sin^2 \theta} \quad (4.12)$$

where t is the plate thickness, k is the thermal conductivity of plate, t_w is the chamber wall thickness, and k_w is the chamber wall thermal conductivity. The stainless-steel plate has thickness t of 0.61 mm. The distance t_w between the thermocouple embedded in the wall and the plate is 3.2 mm. Substituting Equations 2.1 – 2.5 and Equations 4.12 – 4.14 into Equation 4.10 yields the individual droplet heat transfer rate for the experimental setup

$$q_{d,mod} = \frac{\Delta T_{mod} \pi r^2 \left(1 - \frac{r_{min}}{r}\right)}{\frac{\delta/k_{coat} + t/k + t_w/k_w}{\sin^2 \theta} + \frac{r\theta}{4k_c \sin \theta} + \frac{1}{2h_i(1 - \cos \theta)}} \quad (4.13)$$

where δ is the coating thickness, k_{coat} is the coating thermal conductivity, and k_c is the thermal conductivity of condensate. The additional temperature drops result in a reduction of the heat transfer rate through a droplet when compared to the theoretical. The modified small droplet size distribution n_{mod} is dependent on $q_{d,mod}$. It changes only in that coefficient A_3 is replaced with $A_{3,mod}$ defined here as

$$A_{3,mod} = \frac{1}{2h_i} + \frac{1 - \cos \theta}{\sin^2 \theta} \left(\frac{\delta}{k_{coat}} + \frac{t}{k} + \frac{t_w}{k_w} \right) \quad (4.14)$$

The modified distributions n_{mod} and N_{mod} (with modified index b_{mod}) are combined with $q_{d,mod}$ to yield modified heat flux q''_{mod} . The unmodified theoretical heat flux q'' in Equation 2.24 is also shown alongside measured data. The measured heat flux q''_{meas} is found by summing the heat transfer contribution of each detected droplet and dividing by the substrate surface area A_s such that

$$q''_{meas} = \frac{\sum q_{d,mod}}{A_s} \quad (4.15)$$

This heat flux neglects heat transfer through droplets smaller than can be measured. Assuming an accurate measurement of droplets within the measurable radius, this underestimates the actual heat flux taking place. It is also desired to obtain an equivalent heat transfer coefficient that accounts for the effect of the coating. The modified heat transfer coefficient is

$$h_{eq,mod} = \left(\frac{\Delta T_{mod}}{q''_{mod}} - \frac{t}{k} - \frac{t_w}{k_w} \right)^{-1} \quad (4.16)$$

$$h_{eq,meas} = \left(\frac{\Delta T_{mod}}{q''_{meas}} - \frac{t}{k} - \frac{t_w}{k_w} \right)^{-1} \quad (4.17)$$

where t is the plate thickness, k is the thermal conductivity of plate, t_w is the chamber wall thickness, k_w is the chamber wall thermal conductivity, and temperature ΔT_{mod} is the measured temperature difference between the saturated steam and chamber wall thermocouples. The subcool temperature is obtained by rearranging Equation 2.25 as follows

$$\Delta T = \frac{q''}{h_{eq}} \quad (4.18)$$

which applies to both the modified and measured heat flux and heat transfer coefficients.

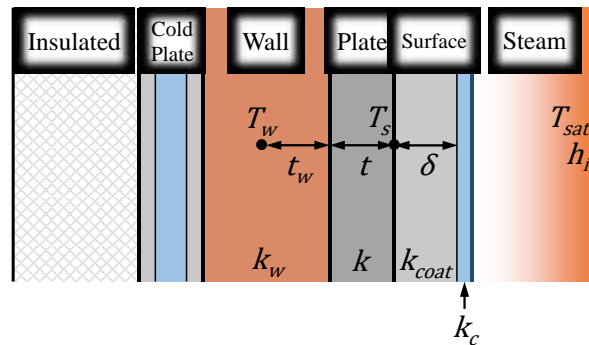


Figure 23. Thermal Resistances for Plate Geometry

The experimental setup of the PC-HEX apparatus involves an externally-insulated cold plate in contact with the chamber wall, upon which a treated plate is mounted. Temperature T_w is the chamber wall temperature, T_s is surface temperature, and T_{sat} is saturation temperature. The thermal conductivity of the condensate is k_c .

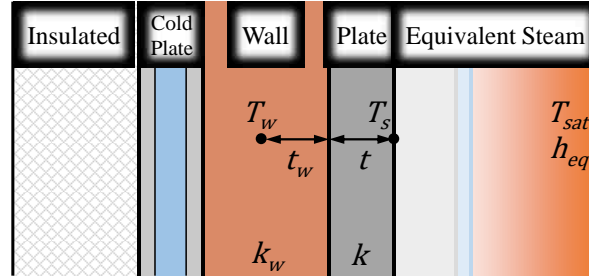


Figure 24. Equivalent Untreated Plate Model

The temperature drops across the coating and condensate layer are lumped into an equivalent heat transfer coefficient h_{eq} .

4.1.4. Measurement Uncertainty

The general approach used for uncertainty analysis is outlined here. For an arbitrary function of three variables $g(x, y, z)$, the absolute uncertainty U_g of g is the root sum square of individual contributions by the independent variables x , y , and z . The relative uncertainty is found as the ratio of the absolute uncertainty to the magnitude of the quantity being considered.

The absolute and relative uncertainty for arbitrary function g are as follows

$$U_g = \sqrt{\left(\left(\frac{\partial g}{\partial x} U_x\right)^2 + \left(\frac{\partial g}{\partial y} U_y\right)^2 + \left(\frac{\partial g}{\partial z} U_z\right)^2\right)} \quad (4.19)$$

$$u_g = \frac{U_g}{g} \quad (4.20)$$

where individual contributions to uncertainty are estimated as the product of the first-order sensitivity of g to changes in that variable and the absolute uncertainty in that variable. The relative uncertainty computation facilitates the comparison of relative contributions to error by quantities with different units. This approach is applied to uncertainty analysis in both the PC-HEX and TC-HEX apparatuses.

Uncertainty in the PC-HEX apparatus propagates from uncertainty in the measurement of droplet radius. A radial uncertainty of one pixel is expected in the droplet detection routine. The

absolute and relative uncertainty in measurement of the droplet radius is U_r and u_r , respectively. The absolute uncertainty in single droplet heat transfer rate is $U_{q_{d,meas}}$. The relative uncertainties in heat flux, equivalent heat transfer coefficient, and subcool temperature are $u_{q''_{meas}}$, $u_{h_{eq,meas}}$, and $u_{\Delta T}$, respectively.

Results of the root sum square uncertainty analysis for relevant quantities in the PC-HEX experimental setup are as follows

$$U_r = \pm 1 \text{ pixel} \quad (4.21)$$

$$u_r = \frac{U_r}{r} \quad (4.22)$$

$$U_{q_{d,meas}} = \left(1 + \frac{A_{3,mod}}{A_2 r + A_{3,mod}} \right) q_{d,meas} u_r \quad (4.23)$$

$$u_{q''_{meas}} = \frac{\sqrt{\sum U_{q_{d,meas}}^2}}{A_s q''_{meas}} \quad (4.24)$$

$$u_{h_{eq,meas}} = \frac{\Delta T_{mod}}{\Delta T} u_{q''_{meas}} \quad (4.25)$$

$$u_{\Delta T} = \sqrt{1 + \left(\frac{\Delta T_{mod}}{\Delta T} \right)^2} u_{q''_{meas}} \quad (4.26)$$

where the sum in Equation 4.24 represents the sum of squared absolute uncertainties $U_{q_{d,meas}}$ for each droplet counted in the detection region. The contribution of uncertainty in ΔT_{mod} to relevant quantities is assumed to be minor compared to the contribution from uncertainty in r . This is because many detections occur near the minimum resolvable radius of four pixels, each of which have a relative uncertainty approaching $\pm 25\%$. Uncertainty in ΔT_{mod} is much less than this. Another assumption made is that the minimum thermodynamically viable droplet radius r_{min} is insignificant compared to the radius r being measured. This is a reasonable

assumption because measured droplets are on the order of millimeters, while the minimum thermodynamically viable radius is on the order of nanometers or smaller.

Uncertainty in the droplet detection method is mitigated by applying it to equivalent transformations of the video data. The method is applied four times, once each on the original video as well as vertically-, horizontally-, and diagonally-mirrored transformations of the video. The mean of four trials reduces the directionality of the method and gives a better estimate of the droplet size distribution. It is more robust, but too complex for the purposes of this study, to detect droplets in overlapping sub-regions within the frame, which would also result in sampling each area four times but reduce the maximum array size handled at one time.

4.2. TC-HEX Data

Coolant temperature and ambient measurements from the TC-HEX apparatus yield the heat flux through a sample. A modification of the single droplet heat transfer model is developed to account for additional thermal resistances in the TC-HEX apparatus. The measured heat flux is compared to the theoretical heat flux from this modified single droplet heat transfer equation. The propagation of measurement uncertainty is also considered.

4.2.1. Relating Measurements to Theory

Measuring the temperature just beneath the coating surface is not performed in the TC-HEX apparatus. Instead, average coolant temperature is measured. Convection by the coolant and conduction to the tube are considered when finding heat flux and subcool temperatures. A cross-sectional view of the tube is shown in **Figure 25**, and the radial, one-dimensional heat transfer problem is defined as in **Figure 26**.

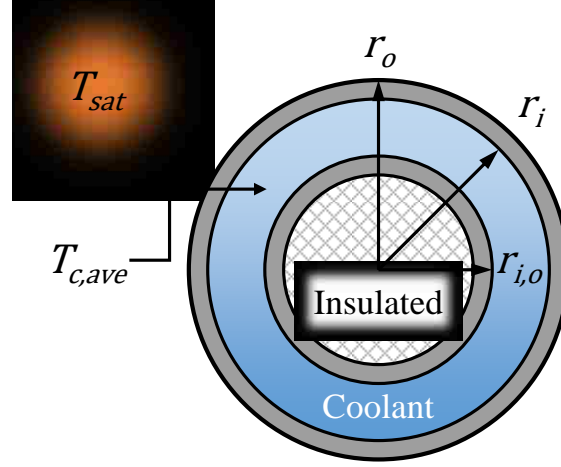


Figure 25. TC-HEX Tube Sample Cross-Section

A cross-section of the tube sample. The outer radius of the inner tube $r_{i,o}$ is 4.76 mm. The inner radius of the outer tube r_i is 7.05 mm. The outer radius of the outer tube r_o is 7.94 mm. The length L (into the page) is 533 mm.

Additional temperature drops are introduced to relate the measured coolant temperature to the surface temperature. The coolant temperature $T_{c,ave}$ is obtained as the average of inlet and outlet coolant temperatures. The overall temperature drop from saturation temperature T_{sat} to the coolant temperature $T_{c,ave}$ is

$$\Delta T_{mod} = \Delta T + \Delta T_t + \Delta T_c = T_{sat} - T_{c,ave} \quad (4.27)$$

with subcool temperature ΔT defined in Equation 2.1 with $q_{d,mod}$ in place of q_d , temperature drop through the tube ΔT_t , and temperature drop through the coolant ΔT_c

$$\Delta T_t = \frac{q_{d,mod} r_o \ln(r_o/r_i)}{k \pi r^2 \sin^2 \theta} \quad (4.28)$$

$$\Delta T_c = \frac{q_{d,mod} r_o}{h_c r_i \pi r^2 \sin^2 \theta} \quad (4.29)$$

where r_o is outer radius of the outer tube, r_i is the inner radius of the outer tube, k is the thermal conductivity of the outer tube, and h_c is the coolant side heat transfer coefficient. Tube curvature is assumed to not change the droplet contact area appreciably. The coolant side heat transfer

coefficient h_c is obtained from a correlation by Gnielinski [41] with friction factor obtained from Petukhov [42]. Substituting Equations 2.1 – 2.5 and Equations 4.28 – 4.29 into Equation 4.27 yields the individual droplet heat transfer rate for the experimental setup

$$q_{d,mod} = \frac{\Delta T_{mod} \pi r^2 \left(1 - \frac{r_{min}}{r}\right)}{\frac{\delta/k_{coat} + r_o(\ln(r_o/r_i)/k + 1/(h_c r_i))}{\sin^2 \theta} + \frac{r\theta}{4k_c \sin \theta} + \frac{1}{2h_i(1 - \cos \theta)}} \quad (4.30)$$

The modified small droplet size distribution n_{mod} is dependent on $q_{d,mod}$. It changes only in that coefficient A_3 is replaced with $A_{3,mod}$ defined here as

$$A_{3,mod} = \frac{1}{2h_i} + \frac{1 - \cos \theta}{\sin^2 \theta} \left(\frac{\delta}{k_{coat}} + r_o \left(\frac{\ln(r_o/r_i)}{k} + \frac{1}{h_c r_i} \right) \right) \quad (4.31)$$

The modified distributions n_{mod} and N_{mod} (with modified index b_{mod}) are combined with $q_{d,mod}$ to yield modified heat flux q''_{mod} . The unmodified theoretical heat flux q'' in Equation 2.24 is also shown alongside measured data. The measured heat flux q''_{meas} is found as the heat transfer into the coolant divided by the outer area of the outer tube

$$q''_{meas} = \frac{\dot{m}_c c_{p,c} (T_{c,o} - T_{c,i})}{2\pi r_o L} \quad (4.32)$$

where \dot{m}_c is 150 g/s, r_o is 7.94 mm and L is 533 mm. The measured heat flux for the PC-HEX is limited to those droplets that can be measured, but the heat flux here accounts for all the energy to the system. Assuming an accurate measurement of coolant temperatures, the measured and modified theoretical heat fluxes should be similar.

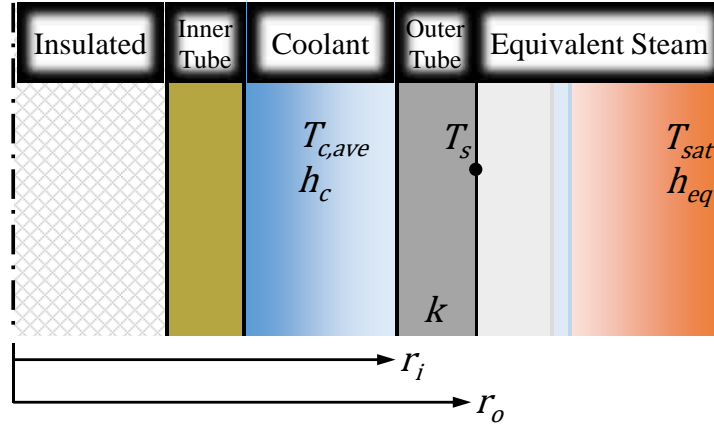


Figure 26. Thermal Resistances for Tube Geometry

The experimental setup of the TC-HEX apparatus involves coolant flowing between an inner and outer tube with steam condensing on the other side of the outer tube. Temperature $T_{c,ave}$ is the average coolant temperature, T_s is the surface temperature, and T_{sat} is saturation temperature.

An equivalent heat transfer coefficient is also defined for the tube geometry. The modified theoretical and measured equivalent heat transfer coefficients are

$$h_{eq,mod} = \left[\frac{\Delta T_{mod}}{q''_{mod}} - r_o \left(\frac{\ln(r_o/r_i)}{k} + \frac{1}{h_c r_i} \right) \right]^{-1} \quad (4.33)$$

$$h_{eq,meas} = \left[\frac{\Delta T_{mod}}{q''_{meas}} - r_o \left(\frac{\ln(r_o/r_i)}{k} + \frac{1}{h_c r_i} \right) \right]^{-1} \quad (4.34)$$

where r_o is outer radius of the outer tube, r_i is the inner radius of the outer tube, k is the thermal conductivity of the outer tube, r_i is the outer radius of the inner tube, and h_c is the coolant side thermal conductivity. Temperature ΔT_{mod} is the measured temperature difference between the saturated steam and average coolant temperature. The subcool temperature is prescribed for theoretical properties and found by Equation 4.18 for measured properties.

This equivalent heat transfer coefficient is also compared to the Nusselt correlation for filmwise condensation

$$h_{fwc} = 0.728 \left[\frac{g\rho(\rho - \rho_g)h'_{fg}k_c^3}{2\mu\Delta T r_o} \right]^{0.25} \quad (4.35)$$

$$h'_{fg} = H_{fg}(1 + 0.068Ja) \quad (4.36)$$

where g is the acceleration due to gravity, ρ is the density of condensate, ρ_g is the density of steam, k_c is the thermal conductivity of condensate, μ is the viscosity of condensate, ΔT is the subcool temperature, r_o is the outer radius of the outer tube, H_{fg} is the latent heat of vaporization, and Ja is the Jakob number.

4.2.2. Measurement Uncertainty

The same approach for uncertainty analysis shown in Equations 4.19 and 4.20 is used for the TC-HEX apparatus. The absolute and relative uncertainty in measurement of the coolant temperature difference is $U_{\Delta T_c}$ and $u_{\Delta T_c}$, respectively. The relative uncertainties in heat flux, equivalent heat transfer coefficient, and subcool temperature are $u_{q''_{meas}}$, $u_{h_{eq,meas}}$, and $u_{\Delta T}$.

Results of such analysis for relevant quantities in the TC-HEX experimental setup are as follows

$$U_{\Delta T_c} = \pm(0.15 + 0.002T_{c,ave}) \quad (4.37)$$

$$u_{\Delta T_c} = \frac{U_{\Delta T_c}}{\Delta T_c} \quad (4.38)$$

$$u_{q''_{meas}} = u_{\Delta T_c} \quad (4.39)$$

$$u_{h_{eq,meas}} = \frac{\Delta T_{mod}}{\Delta T} u_{\Delta T_c} \quad (4.40)$$

$$u_{\Delta T} = \sqrt{1 + \left(\frac{\Delta T_{mod}}{\Delta T} \right)^2} u_{\Delta T_c} \quad (4.41)$$

where $U_{\Delta T_c}$ is defined for a Class A RTD. The contribution of uncertainty ΔT_{mod} to relevant quantities is assumed to be minor compared to the contribution from uncertainty in ΔT_c . This is because relative uncertainty is higher for lower temperature differences and ΔT_c is much lower than ΔT_{mod} . Comparison of Equations 4.37 – 4.41 with Equations 4.21 – 4.26 show that the PC-HEX approach will have lower uncertainty than the TC-HEX approach if $u_{q''_{meas}}$ for the PC-HEX is less than that of $u_{\Delta T_c}$ for the TC-HEX.

It can be seen that $u_{\Delta T_c}$ increases with decreasing ΔT_c . At high coolant temperature (i.e. 100°C) and low coolant temperature difference (i.e. 0.5°C), relative uncertainties $u_{\Delta T_c}$, $u_{q''_{meas}}$, and $u_{h_{eq,meas}}$ exceed 70%, and relative uncertainty $u_{\Delta T_c}$ exceed 140%. The relative uncertainty in the same parameters for the PC-HEX are nearly constant across a wide range of subcool temperatures. Determining heat flux by measuring the droplet size distribution may prove more accurate than determining heat flux by measuring coolant temperature differences. This claim depends on the accuracy of the single droplet heat transfer model and the droplet detection method.

Chapter 5. Results

Results are obtained from the PC-HEX apparatus video data by use of the developed theory. The relationship between the theory and droplet contact angle is also considered. Results are compared with those of the TC-HEX apparatus, and discrepancies are discussed. Finally, measurement uncertainty is determined for both apparatuses.

5.1. PC-HEX

The droplet size distribution is obtained from detecting droplets on the surface over many frames of video data. Two processed frames from a video sequence are shown in **Figure 27**. Detections are reliable down to droplets with a four-pixel radius, corresponding to $272\ \mu\text{m}$. The number of edge pixels available for a very small droplet limits the number of votes that can be made towards its center. A lower vote threshold is set to detect such droplets. Too low a vote threshold introduces false positive detections, so a four-pixel minimum radius was chosen.

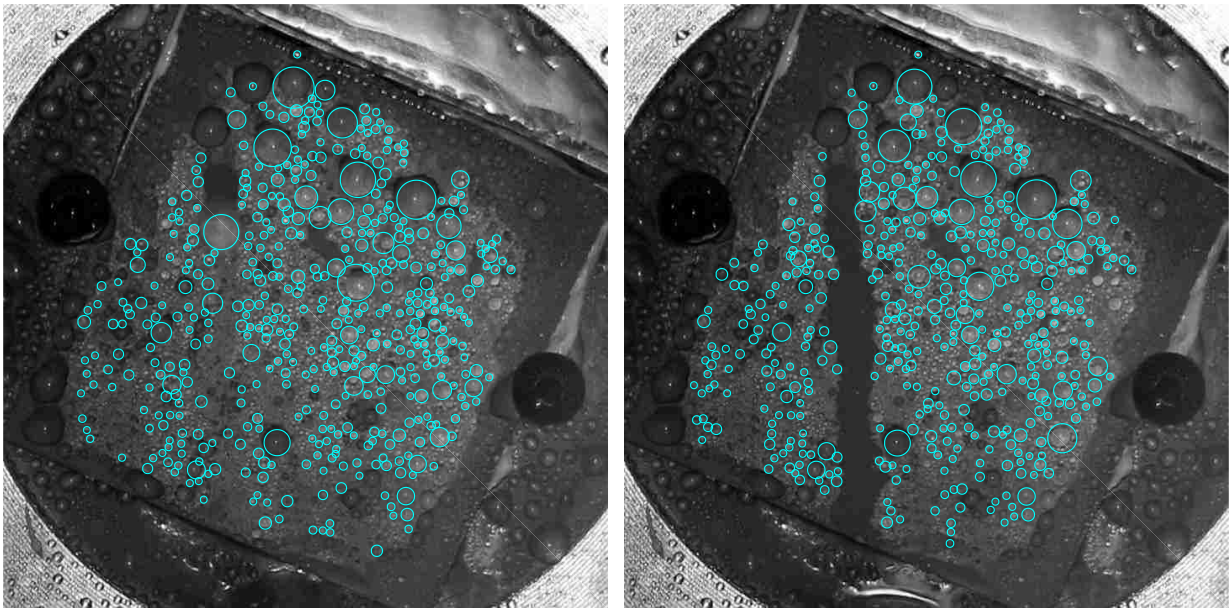


Figure 27. Processed Video Frames Highlighting Droplet Sweeping Event

Left: A processed video frame with a droplet beginning to depart the surface. *Right:* A processed video frame taken 167 ms later. The droplet has swept additional condensate along with it.

Droplet sweeping events occur periodically when a droplet grows large enough to depart the surface under its own weight. The departing droplet entrains any condensate in its path. This exposes the sample surface and allows for droplets to nucleate, grow, coalesce, and eventually be swept again. The plot in **Figure 28** shows sweeping events and the droplet count density over time, with the specific event from **Figure 27** highlighted by a cyan-colored circle. The droplet population increases over time with growth and coalescence, but is reduced by sweeping events.

The droplet size distribution emerges from this balance between droplet growth and sweeping. It gives the count density of droplets of a given radius. It is obtained by binning droplet detections in video data by their radii. Droplet counts in each bin scale with the instantaneous droplet count density shown in **Figure 28**. A representative droplet size distribution is obtained by averaging counts across frames of the video data.

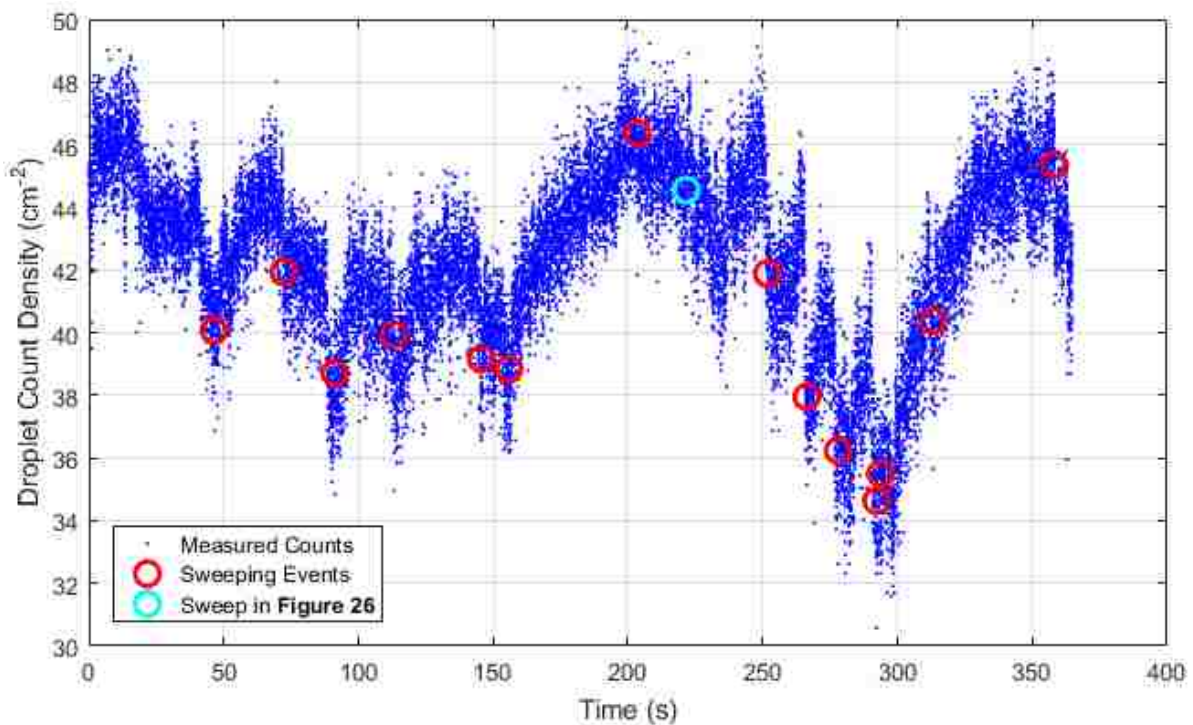


Figure 28. Droplet Count Density and Sweeping Events Over Time

Droplet nucleation causes an increase in droplet count density. Sweeping events cause a decline in the droplet count density.

This representative distribution is shown as the circular data points in **Figure 29**. The bin width used for binning counts is one pixel, or $68 \mu\text{m}$. The measured distribution is compared with the theoretical, where the b index is taken to be $1/3$ from LeFevre and Rose [2]. A nonlinear least-squares fit is also made from the data to the theoretical large droplet size distribution in Equation 2.12 with variable b index. The fitted b index comes out to 0.3320 , resulting in the fitted distribution trending very close to that with a b index of $1/3$. The leftmost circular data point in **Figure 29** is the only data point above the fitted function, but it is at least one order of magnitude larger than most data points below the fitted function. Its deviation above the fitted function offsets all other points deviating below it.

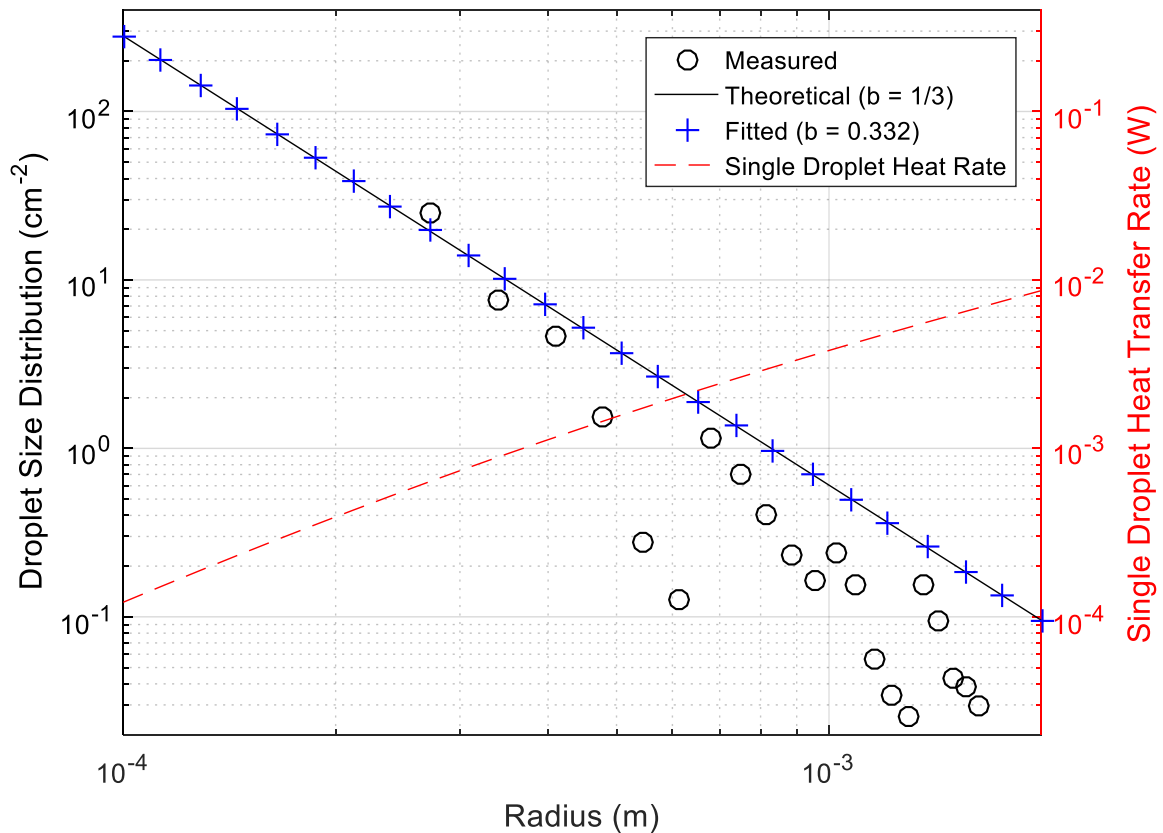


Figure 29. Droplet Size Distribution and Single Droplet Heat Transfer Rate
Left axis: Theoretical, fitted, and measured distributions. A bin width of 1 pixel or $68 \mu\text{m}$ is used.
Right axis: Single droplet heat transfer rate expected at a given radius. The product of this function with the droplet size distribution yields the heat flux at a given radius.

The theoretical single droplet heat transfer rate from Equation 4.13 is also plotted in **Figure 29**, on the secondary axis. The heat flux through the surface is found by integrating the product of the droplet size distribution with the single droplet heat transfer rate. This shows that larger droplets have the greatest influence on the heat flux. Large droplets also appear to be underrepresented in the distribution, which is due to the small area of the sample. The active detection area of the sample is $\sim 10 \text{ cm}^2$, such that bins containing droplets with radii larger than $\sim 500 \text{ }\mu\text{m}$ are expected to have fewer than ten droplets each. A larger sample area would permit more droplets in these bins, yielding a better estimate of the droplet size distribution.

The heat flux is found by summing up the individual heat transfer rate contributions of droplets detected in each frame and dividing by the detection area. This is represented by Equation 4.15. The instantaneous heat flux is also computed for each frame of video data, from Equation 4.17. The results are shown in **Figure 30**. The mean measured heat flux through the measurable range of droplets is found to be 470 W/m^2 . This amounts to about half of the theoretical heat flux measured over the same range. The underrepresentation of larger diameter droplets in **Figure 29** reduces the measured heat transfer relative to the theory. A larger sample area would more adequately represent the largest droplets, thus reducing this discrepancy.

The minimum measurable droplet radius is $272 \text{ }\mu\text{m}$, while the minimum thermodynamically viable droplet radius is on the order of a nanometer. The portion of droplets from about a nanometer to $272 \text{ }\mu\text{m}$ is not captured. This portion of the distribution makes a substantial contribution to heat flux in this model. The total theoretical heat flux predicted from Equation 2.24 is 2.8 kW/m^2 . Only about 17% of the expected heat flux is captured by the measured droplet size distribution. Up to 32% of the expected heat flux may be captured with a large enough sample area. A higher resolution camera would capture more of the heat flux.

Similar observations can be made about the measured versus theoretical equivalent heat transfer coefficient. The measured equivalent heat transfer coefficient is $70 \text{ W/m}^2\text{K}$, while the theoretical value from 4.16 is $410 \text{ W/m}^2\text{K}$. The instantaneous and mean heat transfer coefficients are presented in **Figure 31**. About 32% of the expected equivalent heat transfer coefficient is captured within the measurable range, and the measured value is about 17% of the full $410 \text{ W/m}^2\text{K}$ predicted by theory. A higher resolution camera would capture more droplets, closing the gap between the directly measured and full-distribution heat transfer coefficients.

Additional data for the PC-HEX is shown in **Appendix A**. The dataset captured during the experimental runs that yielded droplet detections from **Figure 22** and **Figure 27** is shown. The video data with overlaid detections is also presented in **Appendix B**. Video data was produced by overlaying circles detected from the modified CHT method onto the original video.

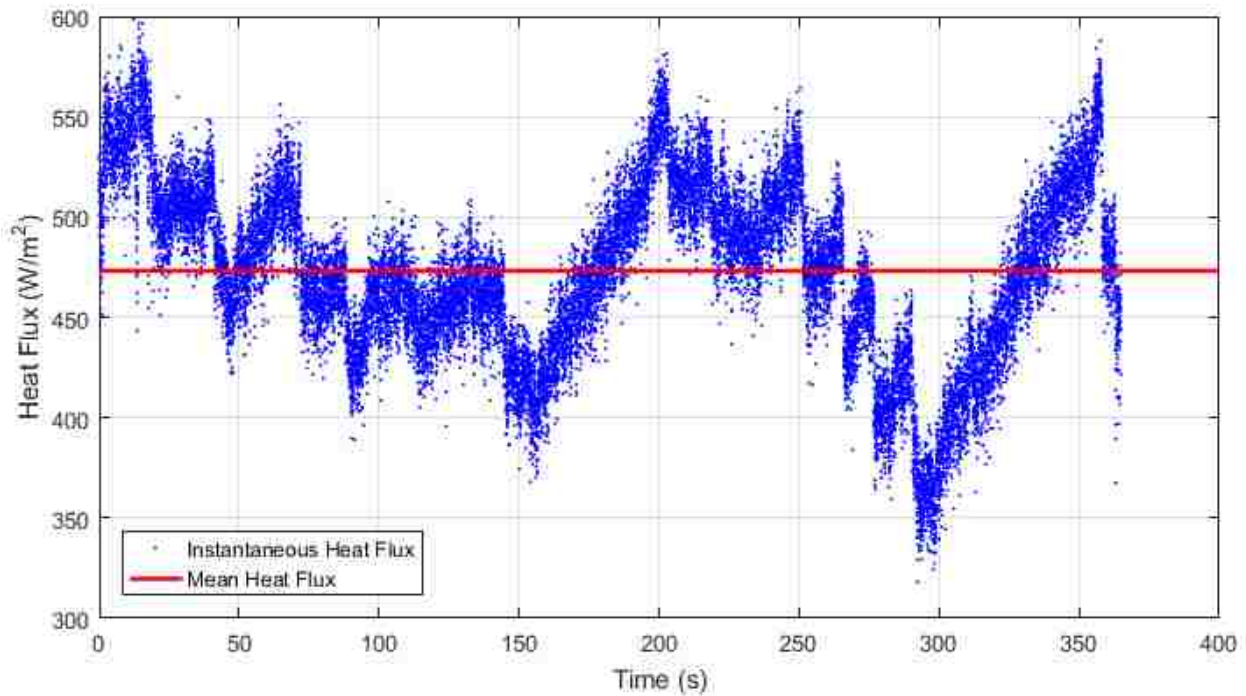


Figure 30. Instantaneous and Mean Heat Flux
Instantaneous and mean heat flux for the video data. The mean heat flux is 470 W/m^2 .

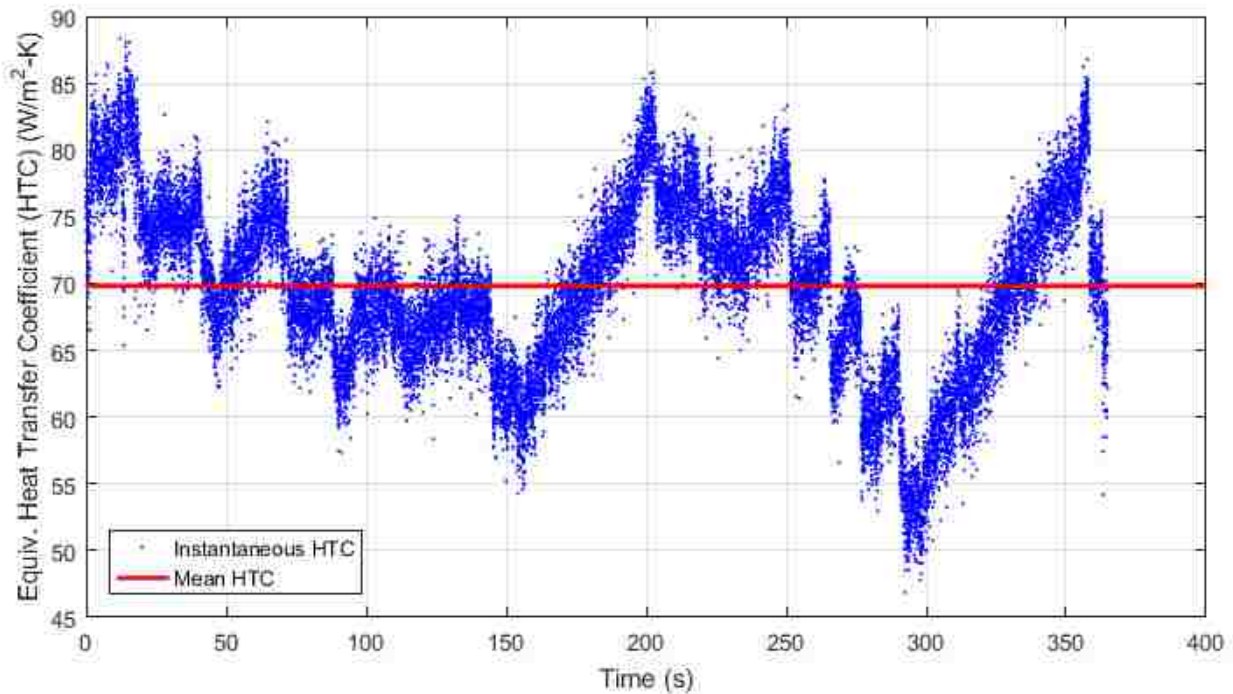


Figure 31. Instantaneous and Mean Equivalent Heat Transfer Coefficient
 Instantaneous and mean equivalent heat transfer coefficient for the video data. The mean equivalent heat transfer coefficient is $70 \text{ W/m}^2\text{K}$.

5.2. Interpretation of Theory

The subcool temperature, from just beneath the coating to saturated steam, is found by the theory to be 6.7 K given a heat flux and equivalent heat transfer coefficient of 470 W/m^2 and $70 \text{ W/m}^2\text{K}$. Since the temperature difference between the wall and saturated steam is 6.8 K , only a 0.1 K additional temperature drop occurs from beneath the coating to the chamber wall. This model predicts dominating thermal resistance somewhere in the coating, condensate, or interfacial layer. Inspection of Equations 2.7, 4.13, and 4.30 reveal that all thermal resistance terms in the denominator approach infinity as contact angle approaches 0° or 180° . This decrease represents the loss of liquid-solid interfacial area as the droplet base shrinks with increasing contact angle. At the same time, obtaining $h_{eq,mod}$ from Equations 4.16 and 4.33 represents the resistances through either the plate/wall or tube/coolant as much smaller than they appear in the

single droplet model. If the additional thermal resistances are neglected, Equations 4.16, 4.18, and 4.33 yield the following

$$h_{eq,mod} \approx \frac{q''_{mod}}{\Delta T_{mod}} \quad (5.1)$$

$$\Delta T = \frac{q''_{mod}}{h_{eq,mod}} \approx \Delta T_{mod} \quad (5.2)$$

which shows the insignificance of the additional temperature drops in the modified temperature drop ΔT_{mod} for both the PC-HEX and TC-HEX apparatuses.

The large thermal resistances in the single droplet model are not offset by the associated increase in the droplet size distribution for increasing contact angle. The droplet size distribution is shown in **Figure 32**. The ratio of the small droplet size distribution for contact angles of 120° and 150° each over 90° is shown. As contact angle increases, the small droplet size distribution first decreases, then increases again. The cross-over angle at ~140° is due to the tradeoff between ratios of A_2 and A_3 over A_1 as they appear in the exponential term within B_1 and B_2 in Equation 2.17.

Even though a small change in droplet size distribution is observed, the marked decrease in single droplet heat transfer rates for increasing contact angle overwhelms this change. This is shown in **Figure 33** as the heat flux distribution, which is the product of the droplet size distribution with q_d . The integral under this curve gives the heat flux, which is equivalent to Equation 2.24. The small droplet size distribution is as much as 1% higher when increasing the contact angle from 90° to 165°. However, the single droplet heat transfer rate drops to about a fifth of its original value given this same change. The heat flux distribution and resulting heat flux is an order of magnitude lower for a contact angle of 165° compared to that of the 90° and 120° contact angles.

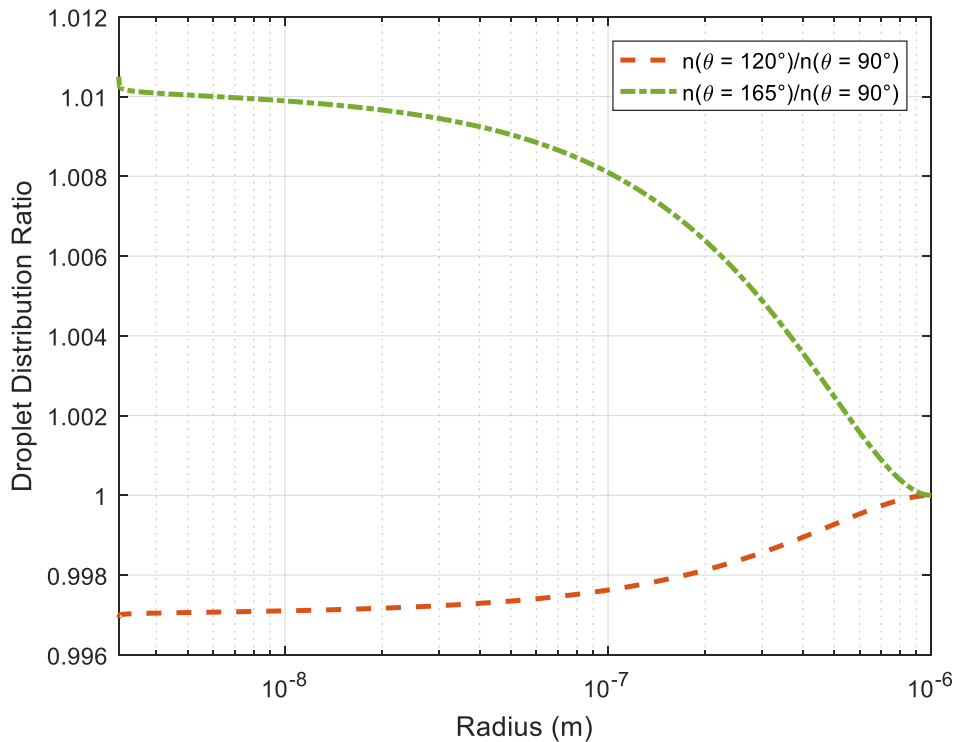
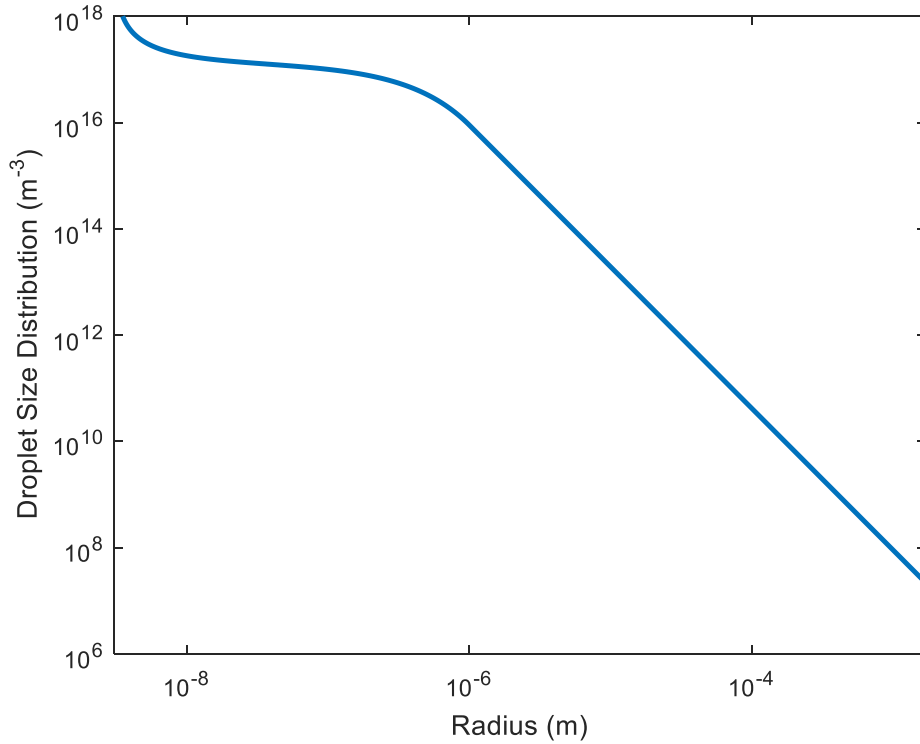


Figure 32. Droplet Distribution and Ratio for Increasing Contact Angle

Top: The droplet size distribution for a contact angle of 90° . *Bottom:* The fractional change in small droplet size distribution for increasing contact angle. The change is less than 2% for a contact angle of 165° versus a contact angle of 90° .

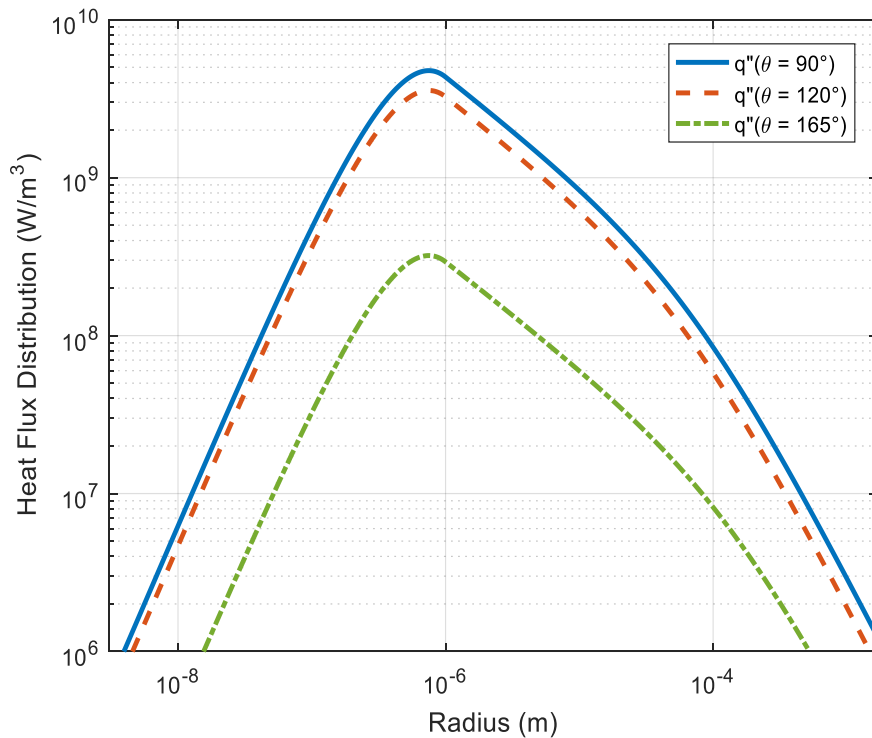
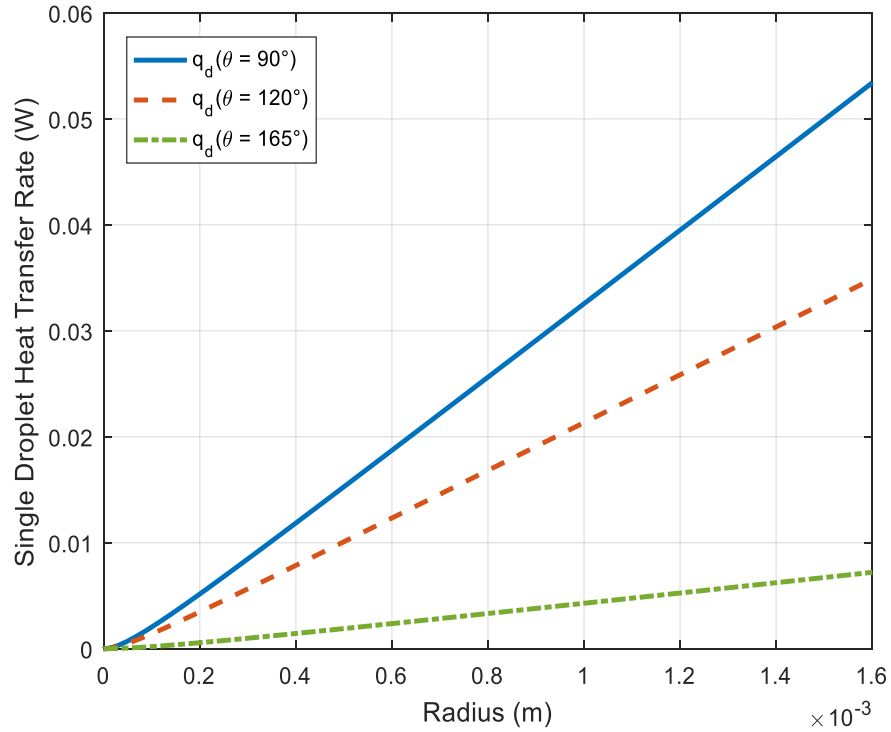


Figure 33. Single Droplet Heat Transfer and the Heat Flux Distribution

Top: The single droplet heat transfer rate decreases as contact angle increases. *Bottom:* The product of the droplet size distribution with single droplet heat transfer rate decreases as contact angle increases.

5.3. TC-HEX

The heat flux measured in the TC-HEX apparatus is much higher than what is measured in the PC-HEX apparatus. The tube samples have the same, PTFE-based coating with the same thickness as the PC-HEX plate sample. The heat flux through the sample over a range of subcool temperatures is shown in **Figure 34**. The expected heat flux for a subcool temperature of 6.7 K is $\sim 75 \text{ kW/m}^2$. The heat flux directly measured in the PC-HEX apparatus is 470 W/m^2 . This can be extrapolated to 870 W/m^2 if considering the small sample size, or 2.8 kW/m^2 if considering the un-measured portion of the distribution. Even though the PC-HEX and TC-HEX apparatuses have slightly different thermal resistances, it would not cause an order of magnitude difference in measured heat flux. This order of magnitude difference is due to the extremely high thermal resistance terms for the single droplet heat transfer rate with a contact angle of 165° .

Similar observations are made for the measured equivalent heat transfer coefficient. The equivalent heat transfer coefficient for the PC-HEX apparatus is $70 \text{ W/m}^2\text{K}$ at 6.7 K subcool temperature. This value might reach $130 \text{ W/m}^2\text{K}$ on a larger sample surface, and the theoretical value across all droplets is $410 \text{ W/m}^2\text{K}$. The equivalent heat transfer coefficient for the TC-HEX apparatus is shown in **Figure 34**. The value is close to $12 \text{ kW/m}^2\text{K}$ for 6.7 K subcool temperature. This difference is similarly attributable to the high contact angle in the model. Also, the equivalent heat transfer coefficient for dropwise condensation is like that of the Nusselt filmwise condensation characteristic for these samples. In this case, the PTFE-based coating is thick enough at $\sim 12 \mu\text{m}$ to offset the heat transfer benefit of dropwise condensation.

Qualitative video data of condensation on TC-HEX sample tubes is comparable to the quantitative video obtained by the PC-HEX. Frames from the video data taken at a subcool temperature of about 6 K are shown in **Figure 35**. Video data is also available in **Appendix B**.

The droplet size distribution observed on the tube geometry is like that observed on the plate geometry, but it is harder to measure because the viewing changes across the tube height.

A temperature difference of 16.6 K between average coolant temperature and saturated steam temperature is set to achieve a subcool temperature around 6.7 K in the PC-HEX apparatus. Using the value of 16.6 K as ΔT_{mod} in Equations 4.30 and 4.40 gives an expected heat flux of 3.9 kW/m² and equivalent heat transfer coefficient of 250 W/m²K, with subcool temperature 16.1 K. The model values are much lower than measured due to the large thermal resistance predicted by the high contact angle.

5.4. Measurement Uncertainty

Measurement uncertainties considered in the PC-HEX apparatus are that of the droplet radius, heat flux, heat transfer coefficient, and subcool temperature. The maximum and mean measurement uncertainties are reported for data plotted in **Figure 28** – **Figure 30**. Droplet radii have 25% and 20% maximum and mean uncertainty. The heat flux and heat transfer coefficient measurements both have 1.2% uncertainty, while the subcool temperature has 1.7% uncertainty.

Measurement uncertainties considered in the TC-HEX apparatus are that of the coolant temperature delta, heat flux, heat transfer coefficient, and subcool temperature. The maximum and mean measurement uncertainties are reported for data plotted in **Figure 34**. The coolant temperature and heat flux both have 21% and 12% maximum and mean uncertainty. The equivalent heat transfer coefficient has 59% and 31% maximum and mean uncertainty. The subcool temperature has 62% and 33% maximum and mean uncertainty. A low measurement uncertainty is needed in both the PC-HEX and TC-HEX apparatuses to be able to reliably compare their results. The uncertainties in both are low enough to back up conclusions made in this study.

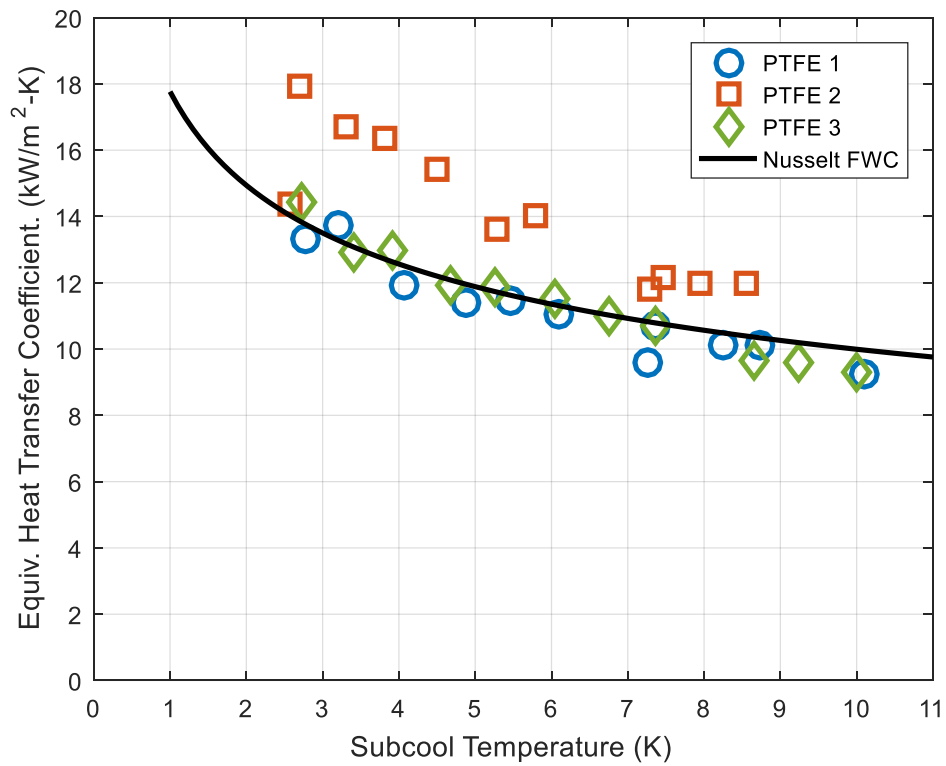
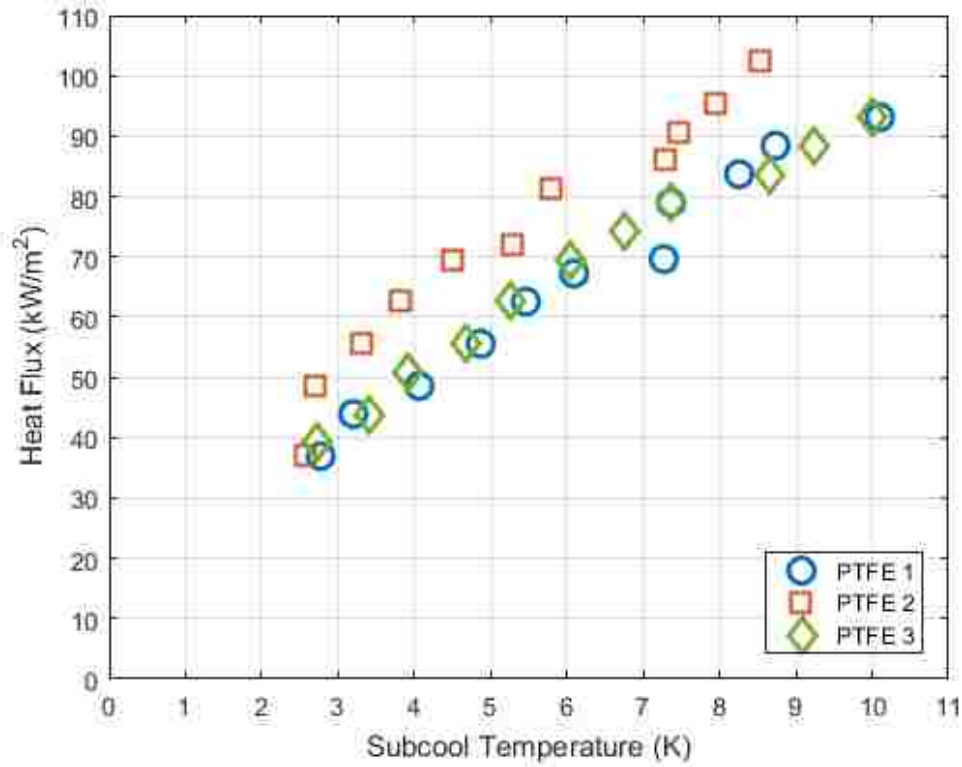


Figure 34. Heat Flux and Equivalent Heat Transfer Coefficient for PC-HEX Tube Samples
 All three samples have the same surface treatment. *Top*: Heat flux for varying subcool temperature. *Bottom*: Equivalent heat transfer coefficient for varying subcool temperature.

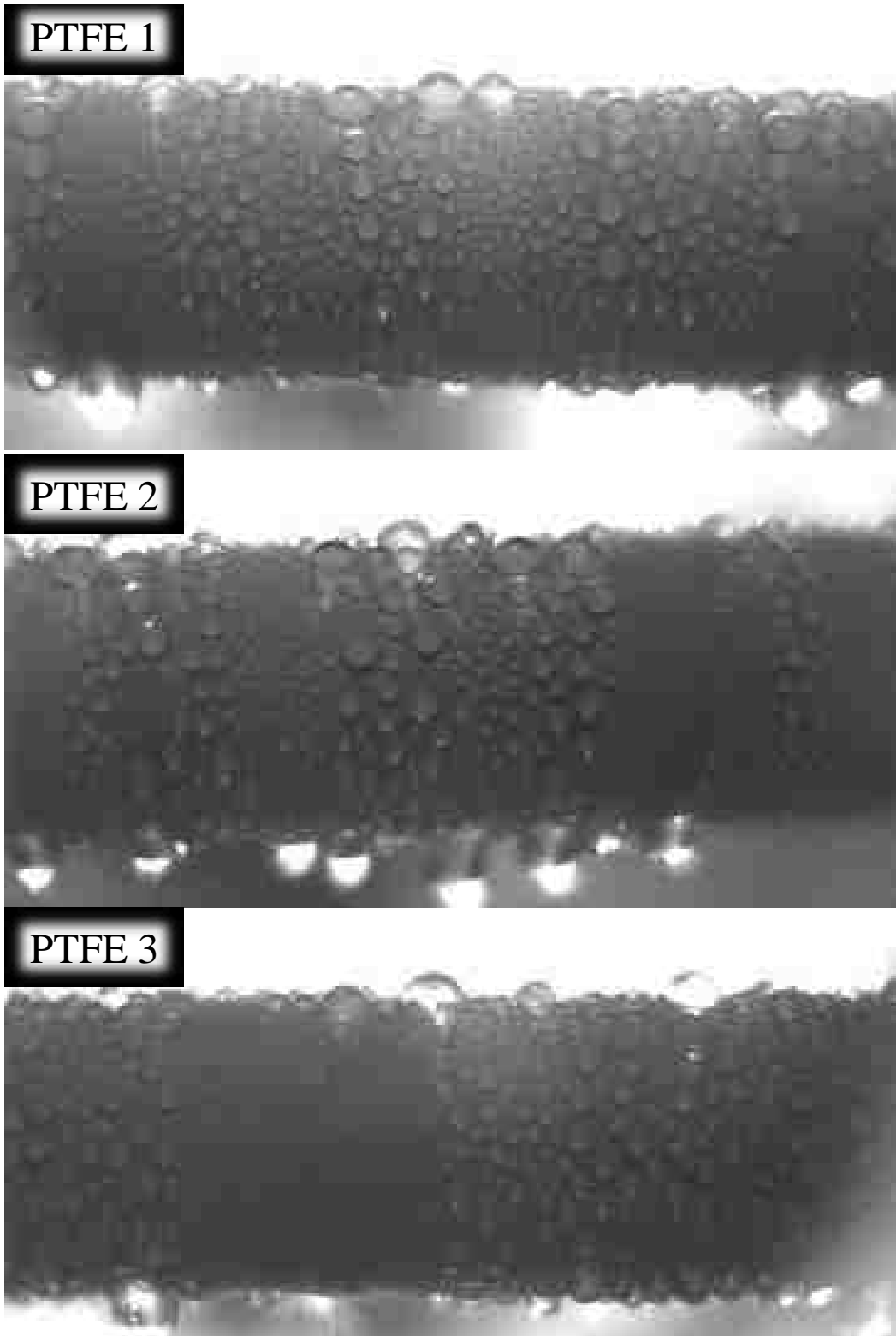


Figure 35. Frame from High-Speed Video Data of PC-HEX Samples
Frame of video data captured of each sample with an inlet coolant temperature of 80°C, corresponding to a subcool temperature of about 6°K. Recent sweeping events control the locally varying maximum droplet radius.

Chapter 6. Conclusion

The relevance of this study lies in the implementation of droplet detection in video data captured from the PC-HEX apparatus. Measurement of the droplet size distribution and the droplet count density over time is made possible by the specially modified CHT. Certain adjustments to the apparatus and detection method are planned in a future study, and another heat transfer model is considered.

6.1. Relevance of Current Study

The ability to measure the condensate droplet population is crucial in the exploration of dropwise condensation heat transfer. Results found in this study agree with the theoretical large droplet size distribution, as shown in **Figure 29**. A decreasing count frequency with increasing droplet radius is observed. Additionally, the experimental setup allows for observation of transient characteristics of the local droplet size distribution. An example of this type of data is presented in **Figure 28**. It is insightful in that it allows for tracking of the mechanisms from which the droplet size distribution emerges. Sweeping events are distinctly visible as an abrupt decline in the droplet count density. Droplets entering the measurable region by growth and coalescence result in the steady rise of the droplet count density when sweeping is not happening. These events correspond directly to real events in the video data.

The TC-HEX apparatus yields heat flux measurements that only depend on the inlet-outlet coolant temperature difference. This provides a result that is independent of the mechanisms that induce the heat flux. While nonspecific, results obtained from the TC-HEX apparatus are used to check those obtained by the PC-HEX apparatus, with its method of heat flux measurement that is mechanism-specific. Quantitative measurement of the droplet size distribution is difficult for video data of the TC-HEX apparatus. As seen in **Figure 35**, the

viewing angle changes across the tube height. While the TC-HEX apparatus yields reliable heat flux measurements, droplet detection is best performed on the plate geometry of the PC-HEX apparatus.

The droplet detection method developed during this study detects droplets with radii that differ by an order of magnitude or more. This is necessary in the measurement of the droplet size distribution. The standard CHT has been modified to take place over multiple stages with vote masking on previously detected circles. This reduces detection noise in the later stages of the process, cutting down on false or missed detections. Another benefit of this method is that it can be used to quickly process time series data. Manual droplet counting may yield a suitable average droplet size distribution, but quickly becomes unmanageable for large image sets.

6.2. Future Study

Refinements to the PC-HEX apparatus and detection method will further improve the ability of the platform to evaluate models of heat transfer by dropwise condensation. The modularity of the apparatus facilitates the planned changes to its sample side and boiler. The underlying detection method established in this study will remain the same, but better memory management will be implemented to handle higher resolution video data. Ground truth verification of droplet counts will also be implemented.

The boiler size limits experimental runtime as seen in **Figure 37** and **Figure 38** in **Appendix A**. Sharp drops in saturation temperature correspond to boiler refills. The 500 cm³ internal boiler has insufficient capacity to run longer than an hour, especially if a larger heating element is used. The boiler flange with an internal boiler will be exchanged for a flange that provides an inlet for an external boiler. The condensate return line will feed condensate back to

the boiler. The rate of heat input will be controllable up to 1 kW, allowing for experimental control over the rate of steam generation.

Fittings that are more appropriate for maintaining vacuum pressure will also be used throughout the apparatus. The leak rate recorded in **Figure 36** in **Appendix A** is sufficiently low for the shorter-duration runs performed in this study. However, longer runs will be possible given a larger boiler. Sensor fittings and ball valves with the appropriate vacuum rating will be used to minimize leak rate. The larger boiler will also ramp up chamber pressure more quickly, minimizing the time spent at low pressure.

The sample side flange will be made to accommodate a larger sample. The largest achievable sample size in the PC-HEX geometry is 80 cm^2 , which is eight times larger than the sample used in this study. Video data will be captured at a resolution of 2160×2160 pixels instead of 720×720 , and a bin width of three pixels ($204 \text{ }\mu\text{m}$) will be used instead of one pixel ($68 \text{ }\mu\text{m}$). With these changes, expected counts in each bin will increase by the ratio of new-to-old sample area. This change guarantees that at least eight counts will occur in bins near the maximum droplet radius. This should mitigate the under-representation of large droplets seen in **Figure 29**. The higher resolution camera will also reduce the minimum measurable droplet radius to below $100 \text{ }\mu\text{m}$, which yields more data for the heat flux estimated by any given single droplet model.

Higher resolution video data requires better memory and processor management. The time taken to run CHT-based droplet detection methods increases exponentially with image size, so large data will need to be broken down into manageable parts. Additional verification of the droplet detection method is also important. While inspection of the detection output is enough to

verify a small sample area at low resolution, actual ground truth verification is needed for larger data sets. These changes will make for a more robust detection method.

6.3. Prospective Heat Transfer Model

One possible approach to heat flux estimation by droplet detection is by monitoring the mass flux of condensate swept from the surface. It has been shown that droplet sweeping events can be detected in a plot of droplet count density over time. These events may be studied further by observing the amount of condensate being swept. Given an assumption of droplet shape and condensate density, a model of single droplet mass is obtained. A combination of this model of droplet mass and the large droplet size distribution shows that 95% of condensate mass is made up by droplets with radii ranging from a tenth of the maximum droplet radius to the maximum droplet radius.

Accumulating the measured mass of droplets in regions that are about to be swept yields the swept condensate mass. Measuring swept condensate mass over time gives the mass flux of condensate. Assuming constant conditions, the mass of condensate stored on the surface should remain constant over time for a large enough sample. Therefore, the mass of condensate being swept over time equals the mass of condensate forming over time. Such a model would allow for heat flux to be inferred from the latent heat change required to form this mass flux of condensate, as well as an expression for the sensible heat change based on residency time.

6.4. Final Remark

The droplet detection method developed in this study has been used to measure droplet population characteristics in the PC-HEX apparatus. These measurements provide insight into mechanisms of dropwise condensation heat transfer, including droplet growth and sweeping. Combining this approach with a given model of single droplet heat transfer and comparing

results to those of the TC-HEX heat exchanger allow for evaluation of the model. Application of the modified CHT droplet detection method also yields transient information about the droplet population. Minor modifications to the apparatus and detection method will contribute to a future study that explores dropwise condensation heat transfer further.

Appendix A: PC-HEX Numerical Data

The PC-HEX chamber is brought down to minimum pressure, and a leak rate is established. The chamber is found to leak at 4 Pa/s. During experimentation, the boiler operates for about an hour before it is vented to atmosphere and the boiler is refilled. The vacuum pump is then used to minimize air pressure before continuing. This ensures that the partial pressure of air in the chamber is no more than 30 kPa during operation.

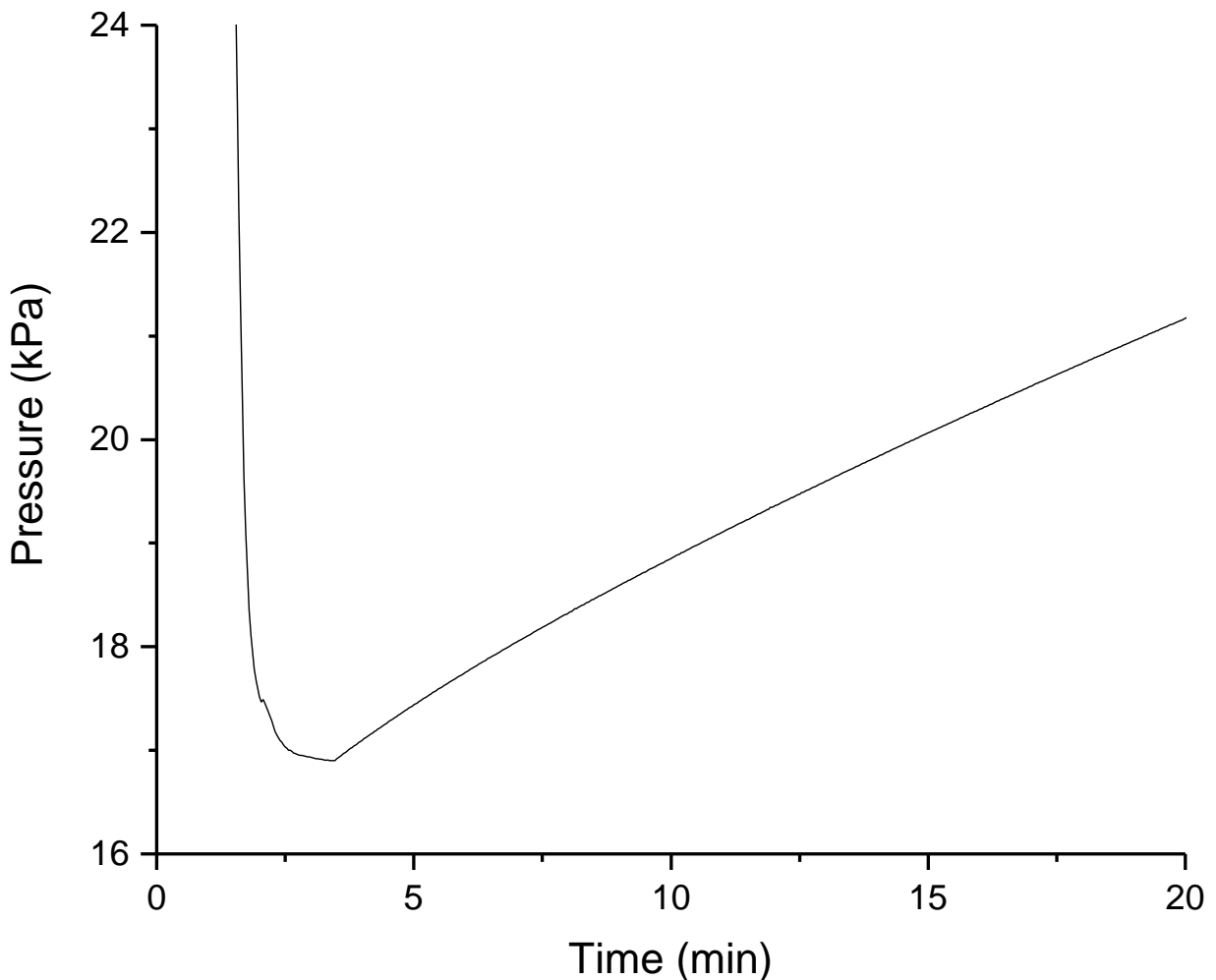


Figure 36. PC-HEX Chamber Undisturbed Pressure

The vacuum pump valve is closed at 3 min, and pressure readings are recorded. Pressure rises over time in the chamber. The leak rate is 4 Pa/s at the low-pressure limit.

Temperature data presented in the experimental run resulting in the capture of frames from **Figure 22** is shown in **Figure 37**. The wall temperature thermocouples report an erroneously high temperature at around 500 s and 7250 s, corresponding to temporarily disabling the data acquisition channel for re-seating of the thermocouples. The frames shown in **Figure 22** were taken around 131 min. The step changes of T_w correspond to changes in chiller set-point to induce variable subcooling. The ramp in T_{sat} corresponds to the 250 W internal boiler slowly ramping up the pressure in the chamber. The periodic decline in saturation temperature corresponds to refilling of the boiler and pumping down of the chamber.

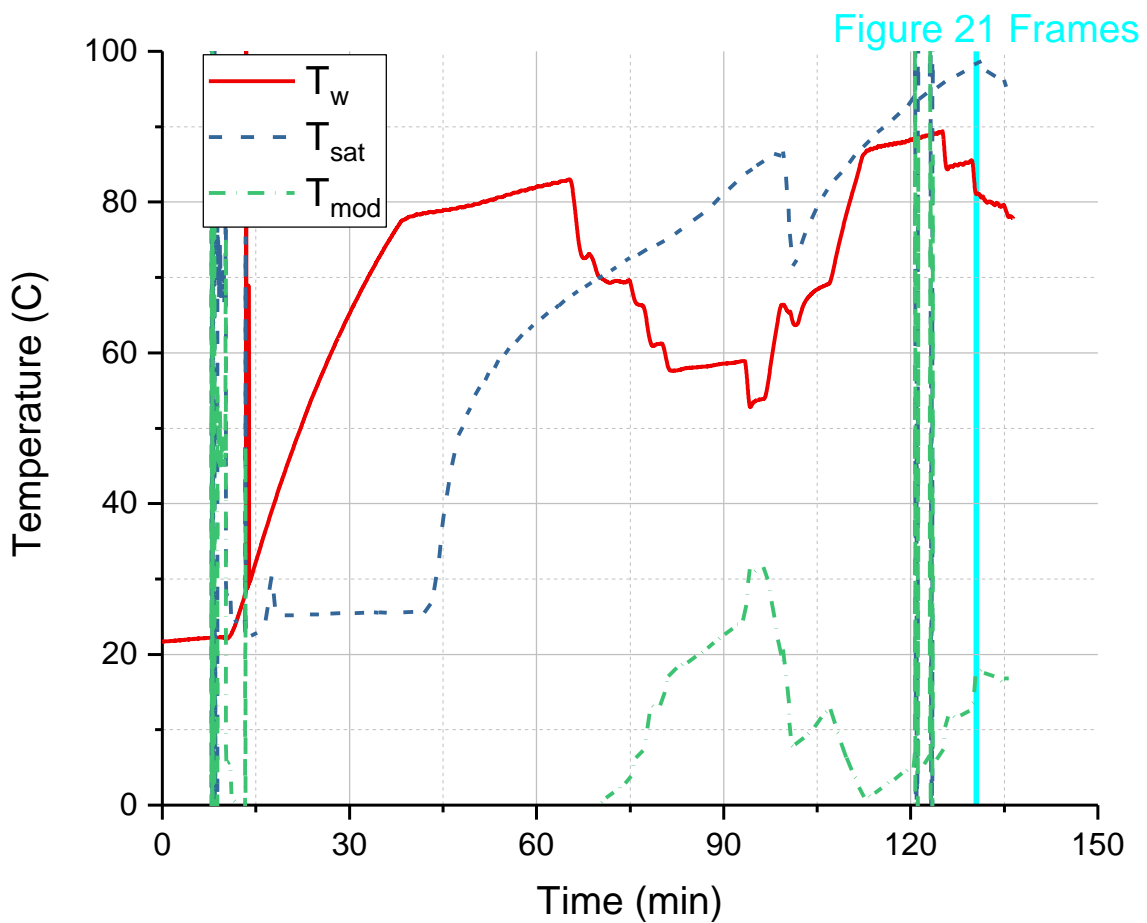


Figure 37. Full Experimental Run for First PC-HEX Sample

This time series shows relevant temperatures gathered during operation of the PC-HEX apparatus. The frames shown in **Figure 22** were captured around 131 min.

Temperature data presented in the experimental run resulting in the capture of frames from **Figure 27** is shown in **Figure 38**. The frames shown in **Figure 27** were taken around 132 min. The step changes of T_w correspond to changes in chiller set-point to induce variable subcooling. The ramp in T_{sat} corresponds to the 250 W internal boiler slowly ramping up the pressure in the chamber. The periodic decline and in saturation temperature corresponds to refilling of the boiler and pumping down of the chamber.

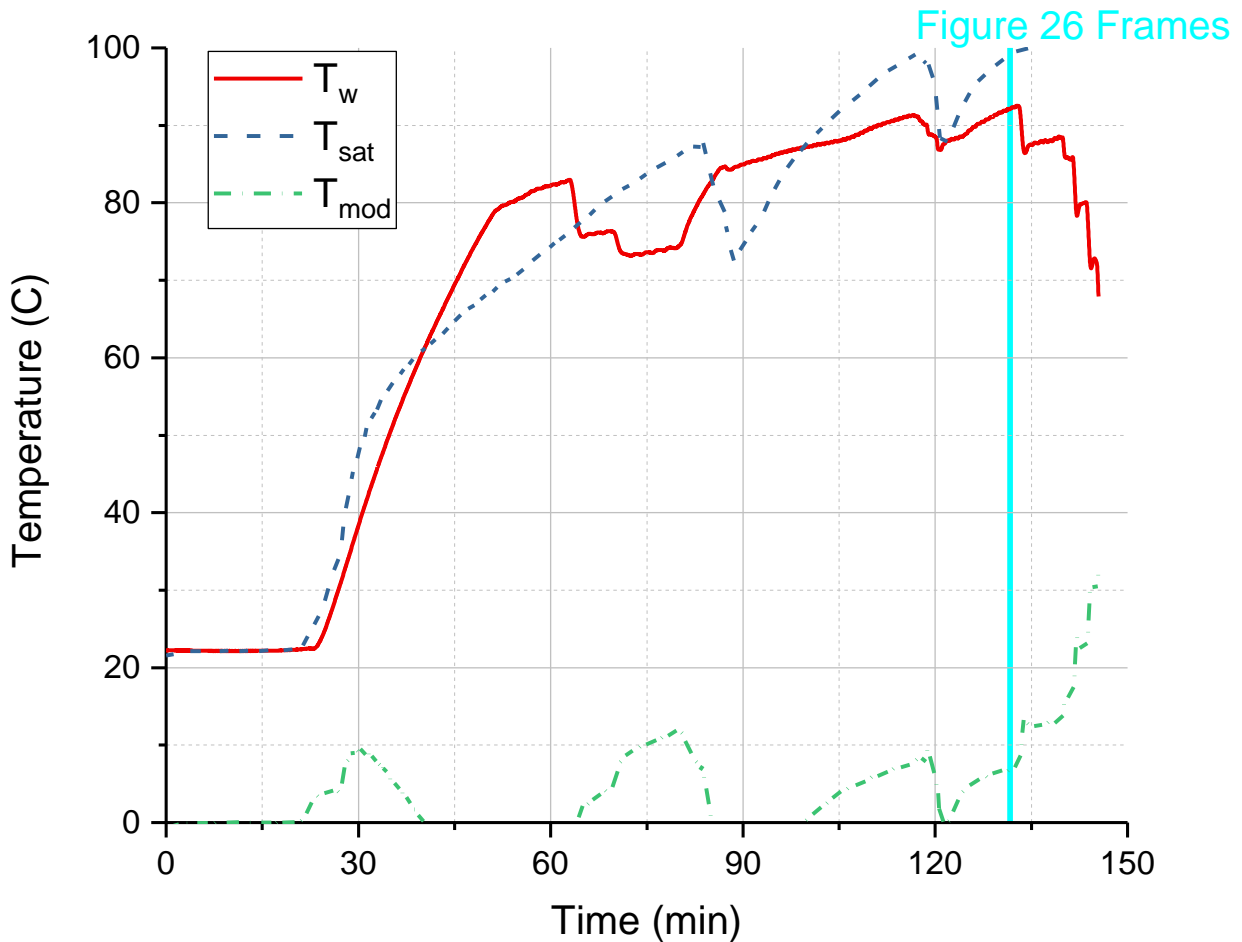


Figure 38. Full Experimental Run for Second PC-HEX Sample

This time series shows relevant temperatures gathered during operation of the PC-HEX apparatus. The frames shown in **Figure 27** were captured around 132 min.

Appendix B: Video Data from the PC-HEX and TC-HEX Apparatuses

Video data is in the attached supplemental material on ProQuest.

Bibliography

- [1] A. Umur, P. Griffith, Mechanism of dropwise condensation, *ASME J Heat Transf.* 87 (1965) 275–282.
- [2] E.J. LeFevre, J.W. Rose, A theory of heat transfer by dropwise condensation, in: *Chem. Eng. Prog.*, AMER INST CHEMICAL ENGINEERS 345 E 47TH ST, NEW YORK, NY 10017, 1966: p. 86.
- [3] E. Schmidt, W. Schurig, W. Sellschopp, Versuche über die Kondensation von Wasserdampf in Film- und Tropfenform, *Tech. Mech. Thermodyn.* 1 (1930) 53–63. doi:10.1007/BF02641051.
- [4] S. Khandekar, K. Muralidhar, *Dropwise Condensation on Inclined Textured Surfaces*, Springer Science & Business Media, 2013.
- [5] T. Young, An essay on the cohesion of fluids, *Philos. Trans. R. Soc. Lond.* 95 (1805) 65–87.
- [6] R.N. Wenzel, Resistance of solid surfaces to wetting by water, *Ind. Eng. Chem.* 28 (1936) 988–994.
- [7] A.B.D. Cassie, S. Baxter, Wettability of porous surfaces, *Trans. Faraday Soc.* 40 (1944) 546–551.
- [8] R.E. Johnson Jr, R.H. Dettre, Contact angle hysteresis. III. Study of an idealized heterogeneous surface, *J. Phys. Chem.* 68 (1964) 1744–1750.
- [9] R.H. Dettre, R.E. Johnson Jr, Contact Angle Hysteresis. IV. Contact Angle Measurements on Heterogeneous Surfaces I, *J. Phys. Chem.* 69 (1965) 1507–1515.
- [10] V.V. Yaminsky, Molecular mechanisms of hydrophobic transitions, *J. Adhes. Sci. Technol.* 14 (2000) 187–233.
- [11] R. Enright, N. Miljkovic, J.L. Alvarado, K. Kim, J.W. Rose, Dropwise condensation on micro- and nanostructured surfaces, *Nanoscale Microscale Thermophys. Eng.* 18 (2014) 223–250.
- [12] S. Vemuri, K.J. Kim, B.D. Wood, S. Govindaraju, T.W. Bell, Long term testing for dropwise condensation using self-assembled monolayer coatings of n-octadecyl mercaptan, *Appl. Therm. Eng.* 26 (2006) 421–429.
- [13] B.J. Zhang, J. Park, K.J. Kim, H. Yoon, Biologically inspired tunable hydrophilic/hydrophobic surfaces: a copper oxide self-assembly multilayer approach, *Bioinspir. Biomim.* 7 (2012) 036011. doi:10.1088/1748-3182/7/3/036011.
- [14] S. Lee, K. Cheng, V. Palmre, M.M.H. Bhuiya, K.J. Kim, B.J. Zhang, H. Yoon, Heat transfer measurement during dropwise condensation using micro/nano-scale porous surface, *Int. J. Heat Mass Transf.* 65 (2013) 619–626.
- [15] B.J. Zhang, C. Kuok, K.J. Kim, T. Hwang, H. Yoon, Dropwise steam condensation on various hydrophobic surfaces: Polyphenylene sulfide (PPS), polytetrafluoroethylene (PTFE), and self-assembled micro/nano silver (SAMS), *Int. J. Heat Mass Transf.* 89 (2015) 353–358.
- [16] G. Azimi, R. Dhiman, H.-M. Kwon, A.T. Paxson, K.K. Varanasi, Hydrophobicity of rare-earth oxide ceramics, *Nat. Mater.* 12 (2013) 315–320.
- [17] D.-J. Huang, T.-S. Leu, Fabrication of high wettability gradient on copper substrate, *Appl. Surf. Sci.* 280 (2013) 25–32.
- [18] C. Lee, D. Kim, Fabrication of patterned surfaces that exhibit variable wettability, *Appl. Surf. Sci.* 288 (2014) 619–624. doi:10.1016/j.apsusc.2013.10.084.

- [19] S. Movafaghi, V. Leszczak, W. Wang, J.A. Sorkin, L.P. Dasi, K.C. Papat, A.K. Kota, Hemocompatibility of superhemophobic titania surfaces, *Adv. Healthc. Mater.* 6 (2017). <http://onlinelibrary.wiley.com/doi/10.1002/adhm.201600717/full>.
- [20] P. Guo, Y. Zheng, M. Wen, C. Song, Y. Lin, L. Jiang, Icephobic/Anti-Icing Properties of Micro/Nanostructured Surfaces, *Adv. Mater.* 24 (2012) 2642–2648.
- [21] S. Lee, H.K. Yoon, K.J. Kim, S. Kim, M. Kennedy, B.J. Zhang, A dropwise condensation model using a nano-scale, pin structured surface, *Int. J. Heat Mass Transf.* 60 (2013) 664–671. doi:10.1016/j.ijheatmasstransfer.2013.01.032.
- [22] N. Fatica, D.L.V. Katz, *Dropwise condensation*, University of Michigan., 1949.
- [23] S. Kim, K.J. Kim, Dropwise condensation modeling suitable for superhydrophobic surfaces, *J. Heat Transf.* 133 (2011) 081502.
- [24] J.W. Rose, Dropwise condensation theory and experiment: a review, *Proc. Inst. Mech. Eng. Part J. Power Energy.* 216 (2002) 115–128.
- [25] C. Graham, *The limiting heat transfer mechanisms of dropwise condensation.*, Massachusetts Institute of Technology, 1969.
- [26] J.W. Rose, L.R. Glicksman, Dropwise condensation—the distribution of drop sizes, *Int. J. Heat Mass Transf.* 16 (1973) 411–425.
- [27] H. Tanaka, A theoretical study of dropwise condensation, *ASME J Heat Transf.* 97 (1975) 72–78.
- [28] A.W. Neumann, A.H. Abdelmessih, A. Hameed, The role of contact angles and contact angle hysteresis in dropwise condensation heat transfer, *Int. J. Heat Mass Transf.* 21 (1978) 947–953.
- [29] J.R. Maa, Drop size distribution and heat flux of dropwise condensation, *Chem. Eng. J.* 16 (1978) 171–176.
- [30] K. Cheng, *Parametric studies on dropwise condensation heat transfer*, University of Nevada, Reno, 2014. <http://search.proquest.com/openview/de3a7b241d97a4a46198eb93cff920d1/1?pq-origsite=gscholar&cbl=18750&diss=y>.
- [31] T.J. Atherton, D.J. Kerbyson, Size invariant circle detection, *Image Vis. Comput.* 17 (1999) 795–803.
- [32] E.R. Davies, *Computer and machine vision: theory, algorithms, practicalities*, Academic Press, 2012.
- [33] I. Tanasawa, *Advances in condensation heat transfer*, *Adv. Heat Transf.* 21 (1991) 55–139.
- [34] D.M. Price, M. Jarratt, Thermal conductivity of PTFE and PTFE composites, *Thermochim. Acta.* 392–393 (2002) 231–236. doi:10.1016/S0040-6031(02)00105-3.
- [35] A. Ranodolph, *Theory of particulate processes: analysis and techniques of continuous crystallization*, Elsevier, 2012.
- [36] S. Vemuri, K.J. Kim, An experimental and theoretical study on the concept of dropwise condensation, *Int. J. Heat Mass Transf.* 49 (2006) 649–657.
- [37] R.O. Duda, P.E. Hart, Use of the Hough transformation to detect lines and curves in pictures, *Commun. ACM.* 15 (1972) 11–15.
- [38] C. Kimme, D. Ballard, J. Sklansky, Finding circles by an array of accumulators, *Commun. ACM.* 18 (1975) 120–122.
- [39] C.M. Thompson, L. Shure, *Image Processing Toolbox: For Use with MATLAB. The MathWorks, Inc Natick MA.* (1993).

- [40] I. Sobel, G. Feldman, A 3x3 isotropic gradient operator for image processing (1968), Talk Stanf. Artif. Intell. Proj. (n.d.).
- [41] V. Gnielinski, New equations for heat and mass transfer in the turbulent flow in pipes and channels, NASA STirecon Tech. Rep. A. 75 (1975) 8–16.
- [42] B.S. Petukhov, Heat transfer and friction in turbulent pipe flow with variable physical properties, Adv. Heat Transf. 6 (1970) 503–564.

Curriculum Vitae

Blake Naccarato

Date Obtained Degree

August 2017 University of Nevada, Las Vegas
(anticipated) M.S. in Mechanical Engineering with Fluids/Thermosciences focus
December 2014 University of Nevada, Las Vegas
B.S. in Mechanical Engineering

Research Focus

Hydrophobic surfaces can promote dropwise condensation in two-phase heat exchange, which improves heat transfer coefficients by an order of magnitude when compared to filmwise condensation. Employing high-speed photography to observe condensate droplet interactions gives insight into this phenomenon.

Publications

- K. Cheng, B. Naccarato, K.J. Kim, A. Kumar, Theoretical consideration of contact angle hysteresis using surface-energy-minimization methods, *International Journal of Heat and Mass Transfer*. 102 (2016) 154–161.
- B. Naccarato, K.J. Kim, High-speed visualization of dropwise condensation heat transfer. Nevada NASA EPSCoR and Space Grant Consortium Annual Meeting (2016). Poster
- B. Naccarato, K.J. Kim, Enhanced condensation via surface modification: Flow visualization. 5th IIR International Conference on TPTPR (2017). Conference Paper.
- B. Naccarato, K.J. Kim, High-speed visualization of dropwise condensation on a bioinspired surface. SPIE Smart Structures/Nondestructive Evaluation (2017). Poster

Honors and Awards

- Awarded the 2015/2016 Higher Education Fellowship by the Nevada NASA Space Grant Consortium
- Graduated *magna cum laude* with University Honors distinction
- Awarded the Graebel Outstanding Student Award for highest GPA in the graduating class of Mechanical Engineering
- Awarded second place in Mechanical Engineering at the UNLV Senior Design Competition for the design and fabrication of a fully automated coffee press prototype

Experience

Dates	Position
2015 – present	Research Assistant, Active Materials and Smart Living Lab, UNLV <ul style="list-style-type: none">• Operating data acquisition tools in an existing two-phase heat exchange setup• Building a vacuum chamber for steam condensation visualization• Utilizing high-speed photography and image processing
2015 – 2016	Teaching Assistant, Engineering Measurements and Controls Laboratory, UNLV <ul style="list-style-type: none">• Prepared and presented signal analysis lectures for the undergraduate lab• Prepared and presented automatic controls lectures for the undergraduate lab
2014 – 2015	Undergraduate Research Assistant, Active Materials and Smart Living Lab, UNLV <ul style="list-style-type: none">• Collected heat transfer data for a horizontal tube two-phase heat exchange setup